Renewable Energy 181 (2022) 870–897

Contents lists available at ScienceDirect

Renewable Energy

journal homepage: www.elsevier.com/locate/renene

Influence of variability and uncertainty of wind and waves on fatigue damage of a floating wind turbine drivetrain

Shuaishuai Wang [a, *], Torgeir Moan [a, b], Zhiyu Jiang [c]

[a] Department of Marine Technology, Norwegian University of Science and Technology (NTNU), Norway
[b] Centre for Autonomous Marine Operations and Systems (AMOS), Department of Marine Technology, NTNU, Trondheim, NO-7491, Norway
[c] Department of Engineering Sciences, University of Agder, N-4898, Grimstad, Norway

ARTICLE INFO

Article history:
Received 19 April 2021
Received in revised form
21 September 2021
Accepted 25 September 2021
Available online 27 September 2021

Keywords:
Semi-submersible floating wind turbine
Environmental variables
Uncertainties
Drivetrain
Fatigue damage

ABSTRACT

This study investigates the effect of variability and uncertainty of wind and wave conditions on the short-term fatigue damage of a 10-MW floating wind turbine drivetrain. Global dynamic responses of a semi-submersible wind turbine are calculated by aero-hydro-servo-elastic simulations in various environmental conditions. Then, rotor and generator loads, as well as nacelle motions from the global analysis are provided to a drivetrain model to investigate its dynamics. One-hour fatigue damage of the drivetrain bearings is calculated based on the bearing loads and speeds, and the effect of uncertainties related to wind and waves is assessed. The results indicate that the variations of mean wind speed, turbulence intensity and wind shear have great effects on the studied drivetrain. The effect of uncertainties of irregular waves on the drivetrain fatigue damage is small. Five wind and wave random samples are sufficient for dynamic analysis of the drivetrain to achieve accurate results at a reasonable computational cost. Among the drivetrain components, the main bearings are generally most sensitive to the investigated environmental variables. Finally, this study discusses the variation of environmental variables in terms of their relative importance for drivetrain analysis. The results provide a basis for establishing improved design standards and engineering practice for design and analysis of floating wind turbine drivetrains.

1. Introduction

The offshore wind energy market has been expanding very fast during the past decade, with an annual increase of nearly 30% between 2010 and 2018 [1,2]. There is a clear trend that offshore wind farms are moving farther into deeper waters from near shore, because high quality and vast untapped offshore wind resources are located in deep water sites [3,4]. Therefore, floating wind turbines (FWTs) are under intensive research and development. Developers have adopted experiences from the oil and gas industry and developed various floating platform technologies [5], which greatly promotes the successful operation of FWTs. Even so, FWTs are still in the precommercial phase of maturity and are anticipated with a significant cost reduction based on their early-stage technology advances and adoptable experiences of technological and commercial developments from bottom-fixed wind turbines [6]. One commonly used measure to reduce the cost is to increase the rotor size and power rating, because larger turbines can harvest more wind energy per unit of area, yield fewer installations, converters, cables, and can lower maintenance costs [6]. Another measure is to increase the reliability and thus to lower the failure rate and extend the service life. To achieve this target, a good understanding of the dynamic response characteristics is a must, as demonstrated by research efforts [7–10].

Among the peer-reviewed studies with respect to dynamic analysis of FWTs, drivetrains have received less attention than other research aspects, e.g., control, hydrodynamics and aerodynamics. Drivetrain is the core part of a wind turbine system which converts the rotor's mechanical energy into electricity. Based on the maintenance and repair data from onshore wind turbines, mechanical components of drivetrains are found to have high failure rates and even worse, these failures often cause significant downtime [11]. According to Caithness Windfarm Information Forum (CWIF) [12], the main causes of wind turbine accidents recorded in the period of 2000–2020 can broadly be categorized as human errors (deficient design, fabrication defects, poor quality

* Corresponding author.
E-mail address: shuaishuai.wang@ntnu.no (S. Wang).

https://doi.org/10.1016/j.renene.2021.09.090

control and maintenance, etc.) and lack of safety margin to cover normal uncertainties, e.g., in environmental conditions. Although there is still limited data to quantify the level of reliability of drivetrains in FWTs, it is important to aim at ensuring a higher reliability in FWT drivetrains. This is also because drivetrains in emerging FWTs are subjected to more complex environmental conditions than those in onshore turbines. Housed in the nacelle of a FWT, a drivetrain is subjected to the fully coupled load effects of wind and waves, control effects of blade pitch, nacelle yaw and generator torque, dynamics of rigid-flexible coupled structure, and nonlinear nacelle motions. Additionally, downtime caused by drivetrain failure in FWTs will result in huge cost loss due to reduced accessibility. Therefore, improving drivetrain reliability is an essential task to achieve the desirable cost reduction of FWTs. There have been a few studies that investigated the dynamic performance of drivetrains in FWTs, e.g., Xing et al. [13], Wang et al. [14], Li et al. [15].

Although these studies give insights into the drivetrain dynamic behavior of FWTs, the dynamic characteristics of drivetrains resulting from uncertainty of turbulent wind and irregular waves are still not yet clarified. Up to now, there is no specific design standard for drivetrains in offshore wind turbines, and current drivetrain design is commonly based on the international standard IEC 61400-4 [16] which refers to the wind turbine design requirements from IEC 61400-1 [17] (onshore) or IEC 61400-3 [18] (offshore). These two standards specify similar wind conditions except wind profile for the design of rotor-nacelle assembly (RNA), and three wind turbine classes are defined in terms of reference wind speed and expected turbulence intensity, under the assumption of neutral atmospheric stability regardless of site locations. Moreover, IEC 61400-3 [18] recommends considering marine conditions, which could reflect an environment at least as severe as those anticipated for offshore wind turbine operations, for the RNA design upon lack of site-specific metocean conditions. Based on IEC 61400-3, the range of wind speeds, significant wave height and spectral peak period are represented by a set of discrete values, with a recommended interval size of 2 m/s for mean wind speed, 0.5 m for significant wave height and 0.5 s for wave spectral peak period. However, it is not clear whether these recommended intervals are appropriate for load effect assessment of drivetrains. Unreasonable resolutions will lead to huge computational efforts associated with a large number of simulations.

As drivetrains in floating wind turbines operate in more complex environmental conditions than their onshore counterparts, many sources of uncertainties exist relating to wind speed, turbulence, shear profile, significant wave height, spectral peak period, and wave direction. However, based on the IEC standards, the minimum safety requirements for drivetrain design of onshore and offshore turbines are the same, implying that the difference in the variability and uncertainties of environmental conditions between onshore and offshore, in particular offshore wind farms, are not taken into account. Therefore, there is an increasing need to improve the current drivetrain design standards, especially for FWTs. In order to contribute towards this goal, a good knowledge of the influence of these uncertainties on the system dynamics of drivetrain is essential.

Motivated by the background described above, the effects of uncertainties in selected environmental parameters on the short-term fatigue damage of a 10-MW drivetrain supported on a semi-submersible floating structure, are addressed in this study. The response is determined by time-domain simulations of a high-fidelity drivetrain dynamic model, where time series of rotor center and generator loads as well as nacelle nonlinear motions are applied. The results demonstrate the relative importance of variability and uncertainty of environmental variables on drivetrain fatigue damage. Moreover, the sensitivity of drivetrain fatigue damage to the uncertainties of the main variables is quantified. Based on this study, a deep insight into drivetrain performance under combined wind and wave conditions is accomplished.

2. 10-MW FWT and drivetrain concepts

2.1. 10-MW FWT concept

A 10-MW semi-submersible FWT is used in the present work. The 10-MW wind turbine was released by the Technical University of Denmark (DTU) Wind Energy in 2013, which is a three-bladed upwind variable-speed collective-pitch turbine. Main specifications of the DTU 10-MW reference wind turbine (RWT) is summarized in Table 1, and additional details can be found in the DTU wind energy report [19]. It is noted that the tower mass in the Table 1 is modified from the original land-based design, to account for the connection with the floating substructure used in this study. More details about the tower modification and the tower properties are introduced in Refs. [20,21].

The 10-MW semi-submersible floating substructure, shown in Fig. 1, was designed by Dr. techn. Olav Olsen AS [22] based on the LIFES 50+ project [23]. The floating substructure has a central column and three outer columns, all of which have a cylindrical upper part and a tapered lower part, which are mounted on a three-legged star-shaped pontoon and a slab is attached to the bottom of the pontoon. Each outer column is connected to the seabed by a catenary mooring line. In each line, a clump mass is attached, which separates the line into two segments. The stretched line length of the upper part and the lower part are 160 m and 543 m, respectively. The main properties of the floating substructure are presented in Table 2. The natural frequencies of the floating wind turbine system are listed in Table 3. More details for the floating substructure and the mooring system are presented in the LIFES50+ project reports [20,21].

2.2. 10-MW wind turbine drivetrain concept

As a promising concept for large-scale offshore wind turbines, a medium-speed drivetrain with a gear ratio of 1:50 was proposed by DTU for the 10-MW wind turbine. The 10-MW medium-speed wind turbine drivetrain used in this study was designed by Wang et al. [25] based on the drivetrain international design standard IEC 61400-4 [16]. The drivetrain employs a traditional four-point support configuration with two main-bearing and two torque-arm supports. Additionally, a three-stage gearbox was designed including two planetary stages and a parallel stage. Fig. 2 presents a schematic layout of the 10-MW wind turbine drivetrain, where the gear and bearing nomenclature and locations are shown. The aerodynamic loads on rotor blades are transmitted to the drivetrain via hub. Ideally, all nontorque loads are transmitted to the tower through the two main bearings and bedplate and will not enter the gearbox. Meanwhile, torque drives the drivetrain to rotate to realize the conversion of mechanical energy to electrical energy.

Fig. 3 shows the topology of the 10-MW wind turbine drivetrain. Ring gears in the first and the second planetary stages are bolted to the gearbox housing. The main shaft is connected to the first stage planet carrier by means of a locking disk; gearbox high-speed shaft is linked to generator by an elastic coupling; spline connection is used between the first and the second stages as well as between the second and the third stages. Torque is input from the rotor side and transmitted serially from hub, main shaft, gearbox low-speed stage to high-speed stage and is output to generator. In the gearbox, planet carriers in the first and the second planetary stages serve as input torque and output torque is applied to the sun gears. In the

Table 1
Main specifications of the DTU 10-MW reference wind turbine [19,20].

parameter	Value
Rating	10-MW
Type	Upwind, 3 blades
Control	Variable speed, collective pitch
Drivetrain	Medium speed, multiple stage gearbox
Cut-in, rated and cut-out wind speed (m/s)	4, 11.4, 25
Cut-in and rated rotor speed (rpm)	6.0, 9.6
Rotor diameter (m)	178.3
Hub height (m)	119.0
Rotor mass (kg)	227962
Nacelle mass (kg)	446036
Tower mass (kg)	1.257E+06

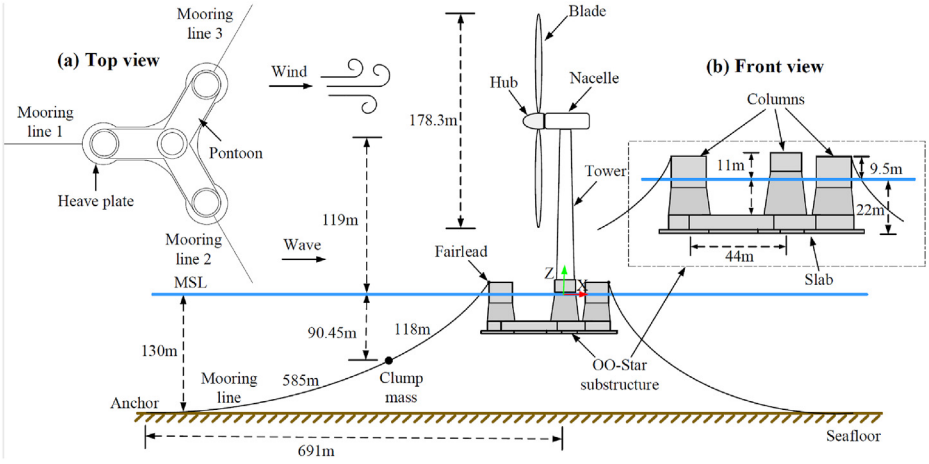

Fig. 1. Sketch of the OO-Star Wind Floater Semi 10-MW concept.

Table 2
Main properties of the OO-Star wind Floater Semi 10-MW floating substructure [20].

Parameter	Value
Water depth (m)	130
Draft (m)	22
Tower base interface above mean seal lever (m)	11
Overall mass, including ballast (× 1000 kg)	21709
Roll and pitch inertia about center of mass (kg·m^2)	9.43E+09
Yaw inertia about center of mass (kg·m^2)	1.63E+10
Center of mass height below mean sea level (m)	15.225
Center of buoyancy height below mean sea level (m)	14.236

third parallel stage, torque is delivered from intermediate shaft to high-speed shaft via the gear pair (Gear-pinion in Fig. 3). Hereby the mechanical energy is transformed from the low-speed and high-torque to high-speed and low-torque form, and the output torque is applied to the generator to generate electricity. Main specifications of the 10-MW drivetrain are listed in Table 4, where the efficiency of the drivetrain is 97.35% which is estimated based on power loss of gear teeth meshing. More detailed information about the drivetrain design and parameters can be found in Refs. [25,26].

3. Analysis methodology

3.1. 10-MW FWT and drivetrain dynamic models

3.1.1. 10-MW FWT dynamic model

The numerical model of the OO-Star wind Floater Semi 10-MW FWT was implemented in an open-source aero-hydro-servo-elastic simulation tool FAST version 8 (v8.16.00a-bjj) [28], which was developed by National Renewable Energy Laboratory. The simulation tool employs a combined multi-body and modal structural approach to account for the structural dynamics of the FWT system. Structural components of the turbine are coupled by means of rigid and flexible bodies. Blades and tower are considered as flexible cantilever beams with continuously distributed mass and stiffness and these structural components are modeled using linear modal representation assuming small deflections. Each blade deflection includes three degrees-of-freedom (DOFs): the first and second flapwise modes as well as the first edgewise mode. The tower deflection includes four DOFs: the first and second fore-aft bending modes as well as the first and second side-to-side bending modes. The floating substructure is represented as a six DOFs rigid body. Mooring lines are established by the lumped-mass approach in the

Table 3
Selected natural frequencies of the 10-MW floating wind turbine system [21,24].

Surge	Heave	Pitch	Yaw	Tower 1st fore-aft	Tower 1st side-side
0.0054 Hz	0.0478 Hz	0.0316 Hz	0.0097 Hz	0.579 Hz	0.746 Hz
185.19s	20.92s	31.65s	103.09s	1.73s	1.34s

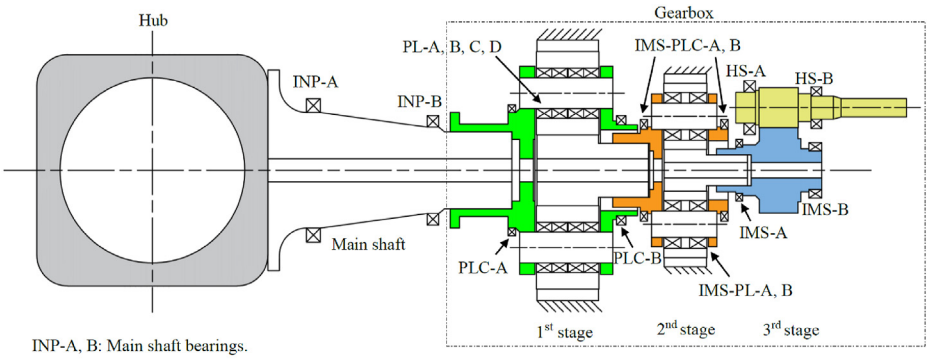

INP-A, B: Main shaft bearings.

PLC-A, B: Planet carrier bearing in the first stage; PL-A, B, C, D: Planet bearings in the first stage.

IMS-PLC-A, B: Planet carrier bearing in the second stage; IMS-PL-A, B: Planet bearings in the second stage.

IMS-A, B: Intermediate shaft bearings in the third stage; HS-A, B: High speed shaft bearings in the third stage.

Fig. 2. 10-MW wind turbine drivetrain schematic layout [25].

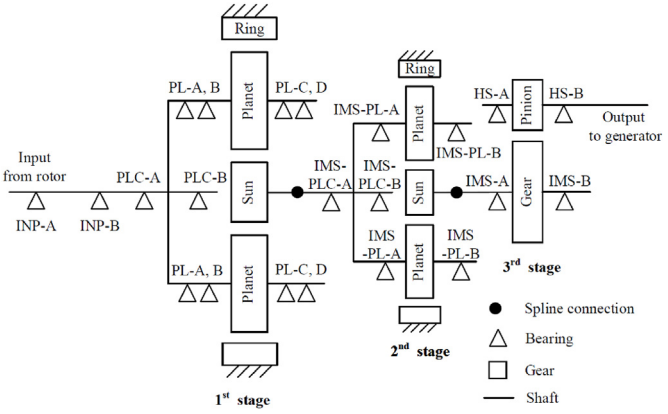

Fig. 3. 10-MW wind turbine drivetrain topology [27].

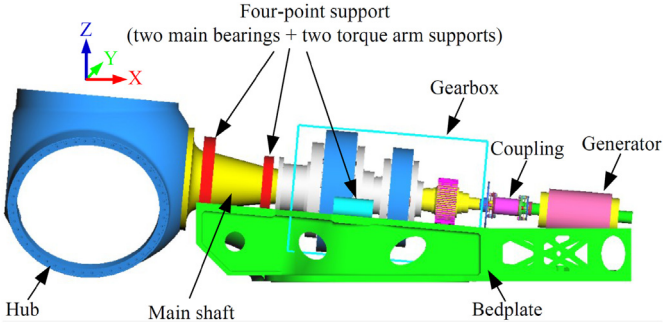

Fig. 4. 10-MW wind turbine drivetrain numerical model [35].

mooring module MoorDyn [29], which is integrated with the FAST simulation tool. In each line, 80 segments are set in the lower part (between clump mass point and anchor point) and 20 segments are set in the upper part (between clump mass point to fairlead point). Each segment of the line has identical dimension and material properties, which are provided in the reference [20].

The drivetrain in the wind turbine model in FAST is modeled as a single DOF torsional spring-damper system. In this system, the rotor and generator are supported on the reference frame with only one rotational DOF, and they are connected to each other by a torsional spring-damper joint. Effective torsional moments of inertia of the rotor and the generator are accounted for considering the drivetrain gear ratio of 1: 50.039.

3.1.2. 10-MW wind turbine drivetrain dynamic model

The dynamic model of the 10-MW drivetrain, shown in Fig. 4, is established by the multi-body system (MBS) method, which is achieved by employing a MBS simulation software SIMPACK (version 2020) [30]. SIMPACK is state-of-the-art dynamic simulation software, which enables users to describe and predict the kinematic and dynamic behavior of complex mechanical or electromechanical system. The key elements of a MBS in SIMPACK consist of body, constraint, joint, external force/moment, force element and coordinate systems, and a physical model of mechanical and mechatronic system is a topological system which is composed of these key elements. The SIMPACK solvers convert the modeling elements and model structures into a set of nonlinear ordinary differential equations (ODE), and additional set of algebraic equations are required to account for constraints or connections, then the complete set of equations are formed as differential-algebraic equations (DAE). The nonlinear DAE set is presented as

Table 4
Main specifications of the 10-MW wind turbine drivetrain [25,26].

Parameter	Value
Drivetrain configuration	Four-point support
Gearbox layout	Two planetary + one parallel
Gearbox total gear ratio	1:50.039
First, second and third stage gear ratio	1:4.423, 1:5.192, 1:2.179
Gearbox dry mass (ton)	60.43
Maximum gearbox outer diameter (m)	3.098
Rated input shaft and generator rotor shaft torque (kNm)	9947.9, 198.8
Drivetrain efficiency	97.35%
Design service life (year)	20

follows [31]:

$$\dot{\boldsymbol{p}} = \boldsymbol{T}(p)\boldsymbol{v} \tag{1}$$

$$\boldsymbol{M}(\boldsymbol{p})\dot{\boldsymbol{v}} = \boldsymbol{f}(\boldsymbol{p},\boldsymbol{v},\boldsymbol{c},\boldsymbol{s},t,\boldsymbol{u},\lambda) - \boldsymbol{G}^T(\boldsymbol{p},\boldsymbol{c},\boldsymbol{s},t,\boldsymbol{u})\lambda \tag{2}$$

$$\dot{\boldsymbol{c}} = \boldsymbol{f}_c(\boldsymbol{p},\boldsymbol{v},\boldsymbol{c},\boldsymbol{s},t,\boldsymbol{u},\lambda) \tag{3}$$

$$0 = \boldsymbol{g}(\boldsymbol{p},\boldsymbol{c},\boldsymbol{s},t,\boldsymbol{u}) \tag{4}$$

$$0 = \boldsymbol{b}(\boldsymbol{p},\boldsymbol{v},\boldsymbol{c},\boldsymbol{s},t,\boldsymbol{u},\lambda) \tag{5}$$

where $\boldsymbol{p}$ are the position states of joints and flexible bodies, $\boldsymbol{T}$ is the transformation of matrix for angles, $\boldsymbol{v}$ are the joint, connection and flexible body states on velocity level, $\boldsymbol{M}$ is the mass matrix, $\boldsymbol{f}$ are the force and torque equations of force elements, $\boldsymbol{c}$ are the dynamic states of force elements, $\boldsymbol{s}$ are the algebraic states on position and acceleration level, t represents time, $\boldsymbol{u}$ are the excitations from joint and connections on position and velocity level, λ are the constraint forces and torques, $\boldsymbol{G}$ denote the Jacobian matrix of the constraint conditions, $\boldsymbol{f}_c$ represent the dynamic state equations of force elements, $\boldsymbol{g}$ represent the algebraic constraint conditions related to constraints, $\boldsymbol{b}$ denote the algebraic constraint conditions related to algebraic states.

The simulation tool has been verified by experimental and code-to-code comparisons in the use of wind turbine drivetrain dynamic analysis [32–34]. The 10-MW wind turbine drivetrain is modeled as a combination of coupled rigid-flexible bodies. Hub, gearbox housing, bedplate and gears are modeled as rigid bodies, while shafts are treated as reduced finite element bodies. Gear teeth meshing forces and bearing forces are calculated by means of two specific force elements in SIMPACK. Gear teeth meshing forces, which account for the stiffness force, the damping force and the friction force, are solved with the input of detailed gear parameters in the gear force element. The six-DOF bearing forces are solved by means of displacement response and the bearing stiffness and damping constant parameters. The dynamic model descriptions and parameters of the 10-MW wind turbine drivetrain are presented in greater detail in Wang et al. [25].

3.1.3. Validation of the 10-MW drivetrain dynamic model

The 10-MW drivetrain dynamic model was validated by a comparison of the drivetrain first-order torsional eigenfrequencies calculated by numerical and theoretical methods, as well as by the resonance check in global and local gearbox perspectives. In the study of Wang et al. [36], the 10-MW high-fidelity drivetrain model was integrated with blades, tower, floating support structure and mooring system, forming a fully coupled FWT dynamic model. Then, the drivetrain first-order eigenfrequency in the global model was calculated by modal analysis in the software SIMPACK; it was then compared with the value calculated based on theoretical method, and the result showed that the difference is less than 5%.

In addition, the drivetrain low eigenfrequencies in non-torsional directions were analyzed in a global perspective, namely focusing on coupled rotor-drivetrain-bedplate-tower modes, and the results showed that the eigenfrequencies in drivetrain first-order vertical and horizontal bending modes are lower than that of the first-order torsional eigenfrequency, but still the resonance was avoided. Besides, in the study of Wang et al. [25], the 10-MW drivetrain, with focus on internal gearbox, resonance analysis was studied. Gearbox shaft rotating frequencies, gear teeth meshing frequencies and their harmonic frequencies, as well as high eigenfrequencies of gear-shaft-bearing coupled modes are plotted in Campbell diagrams, to check the drivetrain's risks for resonance; the results showed that resonance did not occur in this drivetrain model. Based on these studies, it is implied that the 10-MW drivetrain dynamic model is reasonably developed.

3.2. Wind turbine and drivetrain dynamic response analysis

A decoupled analysis method is employed in this study to conduct drivetrain dynamic response analysis. The global aero-hydro-elastic-servo time domain analysis of the OO-Star wind Floater Semi 10-MW FWT is first carried out with a simplified model of the drivetrain in FAST, then the global analysis results are used as input for time-domain dynamic analysis of the high-fidelity drivetrain in SIMPACK. The decoupled analysis method has been effectively used in previous studies, e.g., Refs. [13,27,37]. The fully coupled global analysis and multi-body drivetrain analysis are introduced in more detail in the following sections.

3.2.1. Global aero-hydro-elastic-servo analysis of the 10-MW FWT

The fully coupled global aero-hydro-elastic-servo dynamic analysis is performed in FAST (version8, v8.16.00a-bjj) in the time domain under different environmental conditions. The global responses of the wind turbine are calculated by integrating modules which account for the aerodynamics, hydrodynamics, structural dynamics and controller dynamics.

Aerodynamic loads on blades are calculated in AeroDyn [38], a time-domain aerodynamic module that has been coupled to FAST. In this study, forces and moments on the blades provided by AeroDyn are calculated based on the Blade Element Momentum theory with various advanced corrections, including tip loss, hub loss, Glauert, skewed inflow and dynamic stall corrections [38]. Aerodynamic loads on tower are not considered in the present work.

Hydrodynamic loads acting on the floating substructure are provided by a time-domain hydrodynamic module HydroDyn [39] that has been coupled into FAST. The hydrodynamic loads on the platform include the first-order wave forces and viscous forces, which are calculated by linear potential flow theory and the drag term of the Morison's equation, respectively. Hydrodynamic coefficients, namely added mass and potential damping coefficients, and first-order wave excitation load transfer function are produced in a frequency-domain panel code, WAMIT [40] based on the linear potential theory. The linear frequency-domain motion equation is then transformed into the time domain using a hybrid frequency-time domain approach that was initially introduced by Cummins [41], as shown in Equation (6). Additionally, nonlinear viscous forces on the floating substructure are included through the drag term in the Morison's equation.

$$(M + A_\infty)\ddot{x}(t) + \int_0^t k(t-\tau)\dot{x}(t)d\tau + Cx(t) = F_{exc}(t) \tag{6}$$

where M is the mass matrix of the floating system including rotor, nacelle, tower and substructure, A_∞ is the added mass matrix at infinite frequencies, C is the restoring matrix, which is composed of hydrostatic restoring matrix and nonlinear restoring matrix from the mooring system. $k(t-\tau)$ is the retardation function, which is associated with fluid memory effects and can be found either by the frequency-dependent added mass or potential damping coefficient. $F_{exc}(t)$ is the excitation forces, which include the Froude-Krylov force, diffraction force, aerodynamic force and viscous force.

The hydrodynamic loads acting on the mooring lines are calculated using the Morison's equation. Second- and higher-order wave forces as well as current forces are not included in the present work.

The controller applied to the 10-MW FWT accounts for both the

below rated power and full load region (from rated to cut-out wind speed) operational modes. In the partial load region, the controller is employed for generator torque to obtain an optimal tip speed ratio, intending to achieve maximum power generation. Identical proportional-integral (PI) parameters for the partial load region are employed in the OO-Star wind Floater Semi 10-MW FWT and the DTU 10-MW land-based reference wind turbine. In the full load region, proportional-integral parameters for the blade pitch control are modified from those used on the land-based turbine to avoid the negative damping effects which could result in unstable response of platform motions. Detailed full load region controller parameters are presented in the LIFES50+ project reports [20].

3.2.2. Wind turbine drivetrain load effects analysis

Forces and moments at the hub center, generator speed as well as nacelle motions are extracted from the global analysis. Then, the six-DOF loads are applied at the hub center in the drivetrain dynamic model and the generator torque is controlled on the generator rotor shaft via a proportional integral controller based on the generator speed; the six-DOF nacelle motions (tower top motions) that are represented by displacement, velocity and acceleration are applied at the bottom of the drivetrain bedplate to conduct the drivetrain dynamic analysis. Fig. 5 illustrates the application of hub center and generator loads and nacelle motions on the drivetrain model. Based on the dynamic model and input loads and motions, drivetrain numerical simulations are further conducted and drivetrain bearing load effects are finally obtained.

3.3. Fatigue damage calculation for bearings

Based on previous studies on the load effects of the 10-MW wind turbine drivetrain gears and bearings [14,35], main bearings as well as the gearbox low-speed and high-speed bearings, INP-A, INP-B, PLC-A, PLC-B, HS-A and HS-B are susceptible to wind turbine global load response. Thus, fatigue damage of these six bearings is estimated in this study. The 1-h fatigue damage of bearings is calculated based on the linear damage accumulation theory.

Fig. 6 illustrates the process of creating bearing equivalent load distribution associated with cycles from load time series and load duration distribution. First, the time series of bearing dynamic equivalent load P is calculated based on Equation [42]:

$$P = XF_r + YF_a \tag{7}$$

where F_r and F_a are time series of radial and axial forces on the bearing, respectively, and they are obtained from the drivetrain dynamic simulations. X and Y are bearing dynamic loading factors, which are specified in bearing designations and are selected from the bearing standard ISO 281 [42].

Further, the time series of load P is divided into load bins, which is composed of various load levels P_i and the corresponding duration, as shown in Fig. 6(b). Then, the load duration distribution is transformed to load distribution associated with number of load cycles, as shown in Fig. 6(c). The number of cycles in each bin is calculated by the Equation [25]:

$$l_i = \sum_j \frac{t_j w_j}{2\pi} \tag{8}$$

where l_i is the number of load cycles in the load bin i. t_j is the j-th time duration of the load bin i. w_j is the average bearing inner ring rotational speed (rad/s) in the j-th time duration of the load bin i.

The bearing basic rating life, characterized by the value corresponding to the 10% quantile of the probability density function (PDF) obtained from extensive tests, is expressed by the load-life relationship [42]:

$$L_i = 10^6 \left(\frac{C}{P_i}\right)^a \tag{9}$$

where L_i is basic rating life in the load bin i and is defined as the number of cycles when pitting fatigue damage appears in 10% of the bearings, while the other 90% of bearings work normally in one group test under the load level of the load bin i. C is the bearing basic dynamic load rating, which is a specific constant for one given bearing. a is the bearing life factor, for ball bearings, $a = 3$, and for roller bearings, $a = 10/3$.

Finally, the 1-h bearing fatigue damage accumulated from 200 load bins is calculated according to the Equation:

$$D(EC) = \sum_i \frac{l_i(EC)}{L_i(EC)} = \frac{1}{C^a} \sum_i l_i(EC) \cdot P_i^a \tag{10}$$

where EC represents the environmental condition, which involves the mean wind speed at hub height, turbulence intensity, wind shear exponent, significant wave height, spectral peak period, wind and wave misalignment defined in the Section 3.5. $D(EC)$ is the 1-h accumulative bearing fatigue damage under the environmental condition EC. $l_i(EC)$ is the number of load cycles in the load bin i under EC. $L_i(EC)$ is the number of load cycles to failure in the load bin i under EC. In this study, 200 load bins are used to calculate the 1-h bearing fatigue damage in all cases.

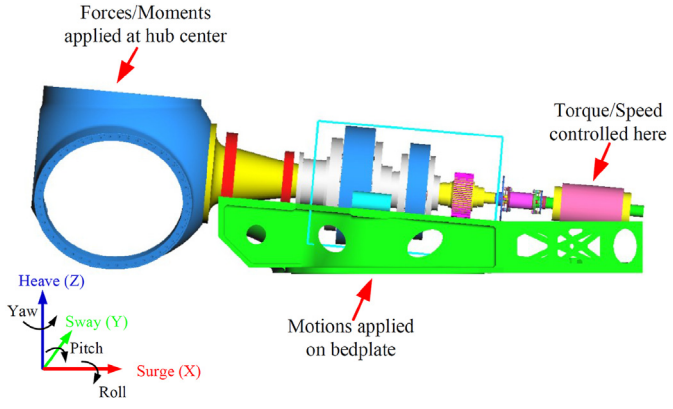

Fig. 5. Application of hub center and generator loads and nacelle motions on the drivetrain model.

3.4. Variability and uncertainties in environmental conditions

Structural reliability measures reflect the effect of uncertainties in the load effects and resistance of the notional failure probability. The variability and uncertainties in load effects depend on those in environmental conditions, modeling of loads and their effect in the wind turbine system. Only the first source of variability and uncertainty is considered herein. The environmental conditions are described by wind, waves and current and their variations in time and space. The variabilities and uncertainties used in practice and in the study in Section 3.5 represent combinations of various sources of variabilities and uncertainties related to wind and waves. This study focuses on fatigue damage of bearings in a drivetrain, which mainly depend on the number of load cycles and magnitude of torque and non-torque loads on the drivetrain shaft. These global responses differ significantly in different operating conditions due to the control strategy. In this study, the variabilities and

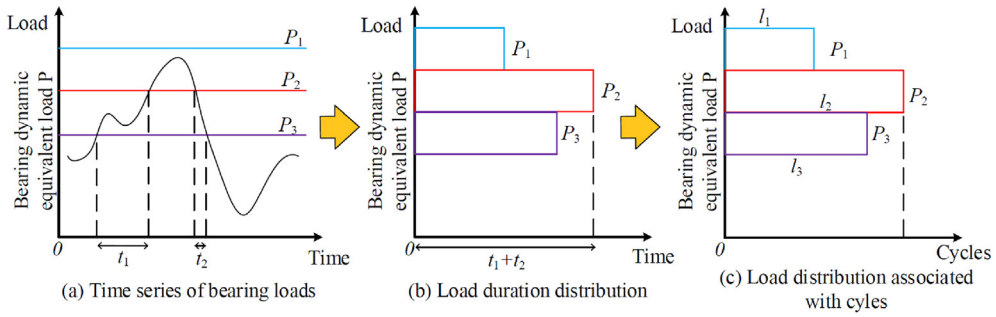

Fig. 6. Process of creating bearing equivalent load distribution associated with cycles from load time series and load duration distribution [27].

uncertainties in wind and wave are addressed in three typical operating regions of the wind turbine.

The variability and uncertainty in wind loads is investigated by considering parameters, namely the mean wind speed, turbulence and wind shear profile. The fundamental uncertainty in mean wind speed is manifested by several short-term wind conditions in a certain range with small intervals of the mean wind speed bin. Turbulence refers to fluctuations in wind speed and its overall level is measured by the turbulence intensity (*TI*), which is defined as the standard deviation of the horizontal wind speed divided by the mean wind speed based on IEC 61400-1 [17]. In the three operating conditions, the normal turbulence model is used, where the standard deviation corresponds to 90% quantile for a given hub height wind speed and is calculated for a wind turbine class. Based on IEC 61400-3 [18], the normal wind speed profile for the standard wind turbine classes is represented by a power law, where the power law exponent is a parameter that represents the level of wind speed shear at a given height. However, the turbulence model and the recommended wind profile model based on the IEC standards are developed under the conditions of neutral stability of the atmosphere and are limited to the surface layer, which cannot represent site-specific metocean conditions. Therefore, the *TI* and reference value of the power law exponent obtained in the models are uncertain and thus are addressed. The wind fields are numerically generated by a turbulence model which combines a spectral model with a spatial coherence model, and the wind field model is also subjected to uncertainties.

The fundamental long-term variability of waves is reflected in a simplified manner by using a few short-term conditions with different significant wave heights and wave spectral peak periods. The basis for these conditions is that they are generated by numerical methods (hindcast) conditioned upon the mean wind speed. Uncertainties also exist in the hindcast model, the meteorological data used in the hindcast model, and the PDF used to represent the long-term variability of the short-term conditions. In addition, the fundamental long-term variability of wind and wave directions is reflected by using four short-term conditions with different wind and wave misalignments. The short-term variability of waves is represented by a directional wave spectrum, which is subjected to model uncertainties.

In addition, the short-term fatigue damage of bearings in a drivetrain should be determined based on a certain number of simulations, which therefore leads to statistical uncertainties. The statistical uncertainty in the realization of short-term wind and wave conditions is addressed by using different numbers of samples.

3.5. Case studies

Based on the above discussions, the variabilities and uncertainties in the mean wind speed, turbulence intensity, wind shear exponent, significant wave height, spectral peak period and wind and wave misalignment as well as the sampling of wind and wave conditions are considered in this study. The 10-MW FWT is assumed to be installed at a representative location, site 14 in the Northern North Sea, which is described in the study of Li et al. [43]. The long-term joint distributions of mean wind speed (u), significant wave height (H_s) and spectral peak period T_p for the site was acquired by fitting 10 years' environmental hindcast data, which are generated based on a numerical hindcast model from the National and Kapodistrain University of Athens. The hindcast data have been sampled hourly for wind and waves from 2001 to 2010.

Long-term fatigue damage of a drivetrain bearing was estimated in the study of Jiang et al. [44], where a total of 41 load cases, 22 operational cases, 13 parked cases and 6 transient cases, with the probability of occurrence of each load case estimated based on IEC 61400-1 [17]. The result shows that the normal operating load cases dominate the long-term fatigue damage of the bearing, while the fatigue damage is less affected by the transient and parked load cases. Thus, only the normal operating conditions are considered in this study. Three reference operating conditions are selected at three hub-height mean wind speeds of 5, 12 and 24 m/s, representing the below-rated, rated and above-rated wind conditions. Fig. 7 shows the marginal distribution of the mean wind speed at hub height, where the selected three operating conditions are marked. In each condition, the most probable significant wave height and spectral peak period are selected according to the conditional distributions for given mean wind speeds. The three operating conditions with turbulent wind and irregular waves are presented in Table 5.

In addition, the most probable values of H_s and T_p are used as the reference values in Table 6.

Table 6 shows the variation ranges and reference values of these environmental parameters in each operating condition. The

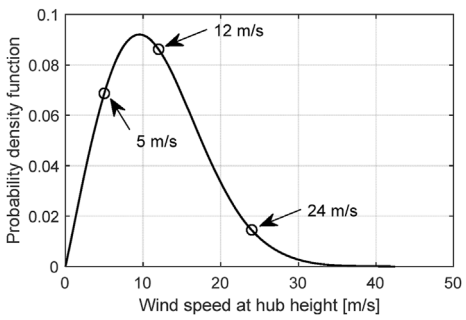

Fig. 7. Marginal distribution of mean wind speed at the hub height of the 10-MW wind turbine.

reference values for the mean wind speed are 5, 12 and 24 m/s, respectively. The TI and wind shear exponent are selected based on the IEC 61400-3 [18]. Their variation ranges are considered from −10% to 10% to reveal the sensitivity in short-term fatigue damage of bearings to the variability of these environmental parameters. The reference values for the significant wave height and spectral peak period in each operating condition are the most probable values, as listed in Table 5, and their variation ranges are considered from 25% to 75% quantile in their long-term probability density distribution. The variation range for the wind and wave misalignment is considered from 0 to 90°, as illustrated in Fig. 35 in Section 4.5, and the 0° is used as the reference value. In addition, the variation range for the number of 1-h samples of wind and waves are considered from 1 to 30 and the number of 30 is used as the reference value. In order to quantify the influence of variability of each environmental parameter on drivetrain fatigue damage, all the other parameters remain the reference values at the time when one parameter varies. More details for the descriptions of these environmental parameters are provided in the next section.

The normal turbulence model and normal wind profile model are used in all the simulations in this study. The Kaimal turbulence model is used to generate three-dimensional time-varying wind fields applying for wind turbine Class C defined in the IEC 61400-3 [18], using a stochastic turbulent-wind simulator, TurbSim [45]. Time-varying irregular short-crested waves are generated using the JONSWAP (Joint North Sea Wave Project) spectrum [18] with given H_s and T_p. Currents are not considered in this study.

Each simulation lasts for 4000s with time step of 0.025s, and the first 400s is removed to eliminate the start-up transient effect, thereby forming a 1-h dynamic simulation. To reduce the stochastic variability, five independent simulations with random samples are conducted in each scenario to get the results in Section 4, except for Section 4.6, where simulations with 30 random samples are performed. As shown in Section 4.5, the statistical uncertainty by using five samples is less than 1–2%.

4. Results and discussions

This section demonstrates the effect of variabilities and uncertainties of turbulent wind and irregular waves on the short-term fatigue damage of drivetrain bearings. As illustrated in Fig. 6 and Eq. (10), the fatigue damage of bearings depends on the bearing dynamic equivalent load P and the corresponding load cycles l, and P serves as the main cause to the fatigue damage due to the power exponent a. The bearing dynamic equivalent load P is calculated based on the bearing radial and axial forces, which are affected by drivetrain shaft loads and nacelle motions. Regarding the effect of drivetrain shaft loads, torque loads dominate the bearing fatigue damage of the gearbox, while nontorque loads determine the fatigue damage of the main bearings. The variabilities and uncertainties of turbulent wind and irregular waves would affect the drivetrain shaft loads, load cycles and nacelle motions according to global analysis and consequently affect the fatigue damage of drivetrain bearings.

Table 5
Operating conditions with turbulent wind and irregular waves.

No.	Operating condition	$u\ (m/s)$	$H_s\ (m)$	$T_p\ (s)$
Condition1	Below-rated	5	1.6	9.4
Condition2	Rated	12	2.5	10.1
Condition3	Above-rated	24	5.4	11.9

Note: in this table, most probable values of H_s and T_p are presented for a given wind condition and they correspond to different quantiles depending upon the PDF of the variable.

Table 6
Variation ranges and reference values of environmental parameters in each operating condition.

Environmental parameters	Variation range	Reference value
Mean wind speed	−10% to +10%	5, 12 and 24 m/s
Turbulence intensity	−10% to +10%	[a]Calculated by IEC-Class C
Wind shear exponent	−10% to +10%	0.14
Significant wave height	25%–75% quantile	Presented in Table 5
Spectral peak period	25%–75% quantile	Presented in Table 5
Wave misalignment	0–90°	0°
Number of samples	1 to 30	30

[a] : reference value of turbulence intensity for each wind speed condition is calculated based on Eqs. (12) and (13) in Section 4.2 according to IEC-Class C, where turbulence intensity is estimated based on IEC 61400-1 [17] for wind turbine Class C.

4.1. Effect of variability of the mean wind speed

In this section, the effect of variability of the mean wind speed on drivetrain fatigue damage in different environmental conditions are studied. The short-term fatigue damage and the corresponding probability of occurrence of environmental conditions determine the long-term fatigue damage of the wind turbine structure for a specific offshore site. The probability of occurrence of each environmental condition can be obtained from the long-term joint probability distribution of u, H_s and T_p, which is established based on hindcast data for a specific site, as described in the study of Li et al. [43]. The IEC 61400-3 [18] standard recommends that the interval of mean wind speed bin shall be 2 m/s in the joint probability distribution. However, whether the resolution is acceptable for the assessment of drivetrain fatigue damage is not clarified. In order to shed light on this issue, the variations of 1-h fatigue damage of drivetrain bearings resulting from the variations of mean wind speed in different operating conditions are investigated.

Fig. 8 illustrates the variation of performance of global responses, including blade pitch angle, generator speed as well as forces and moment at hub center, with mean wind speed in the whole operating range from cut-in to cut-out. Under each mean wind speed condition, *TI* and wind profile exponent are considered based on the IEC 61400-3 [18]; the most probable significant wave height and wave spectral peak period are selected from the conditional distributions and collinear wind and waves are considered based on the wind direction. Each curve is fitted by response statistics, based on 5 1-h simulations, of 22 wind speed conditions with an increment of 1 m/s.

The rated wind speed corresponds to 11.4 m/s. Below this condition, the rotor torque and speed increase with the mean wind speed to realize maximum power output. Above this condition, the blade pitch controller is activated, and blade pitch angle increases for increasing mean wind speed to realize constant torque. Large standard deviations are observed in bending moments *My* and *Mz* of the drivetrain shaft, especially in high wind speed conditions, as shown in (g) *My* and (h) *Mz* in Fig. 8, which is induced by low frequency wind turbulence and the rotor 3P and 6P excitations. The generator speed and torque and nontorque loads of the drivetrain shaft serve as the basis for assessments of the fatigue damage of drivetrain bearings.

Table 7 – 9 demonstrate the effect of the variation of mean wind speed on the drivetrain 1-h fatigue damage under the below-rated, rated and above-rated operating conditions, respectively. The variation in bearing 1-h fatigue damage is expressed by percentage difference, χ, defined as:

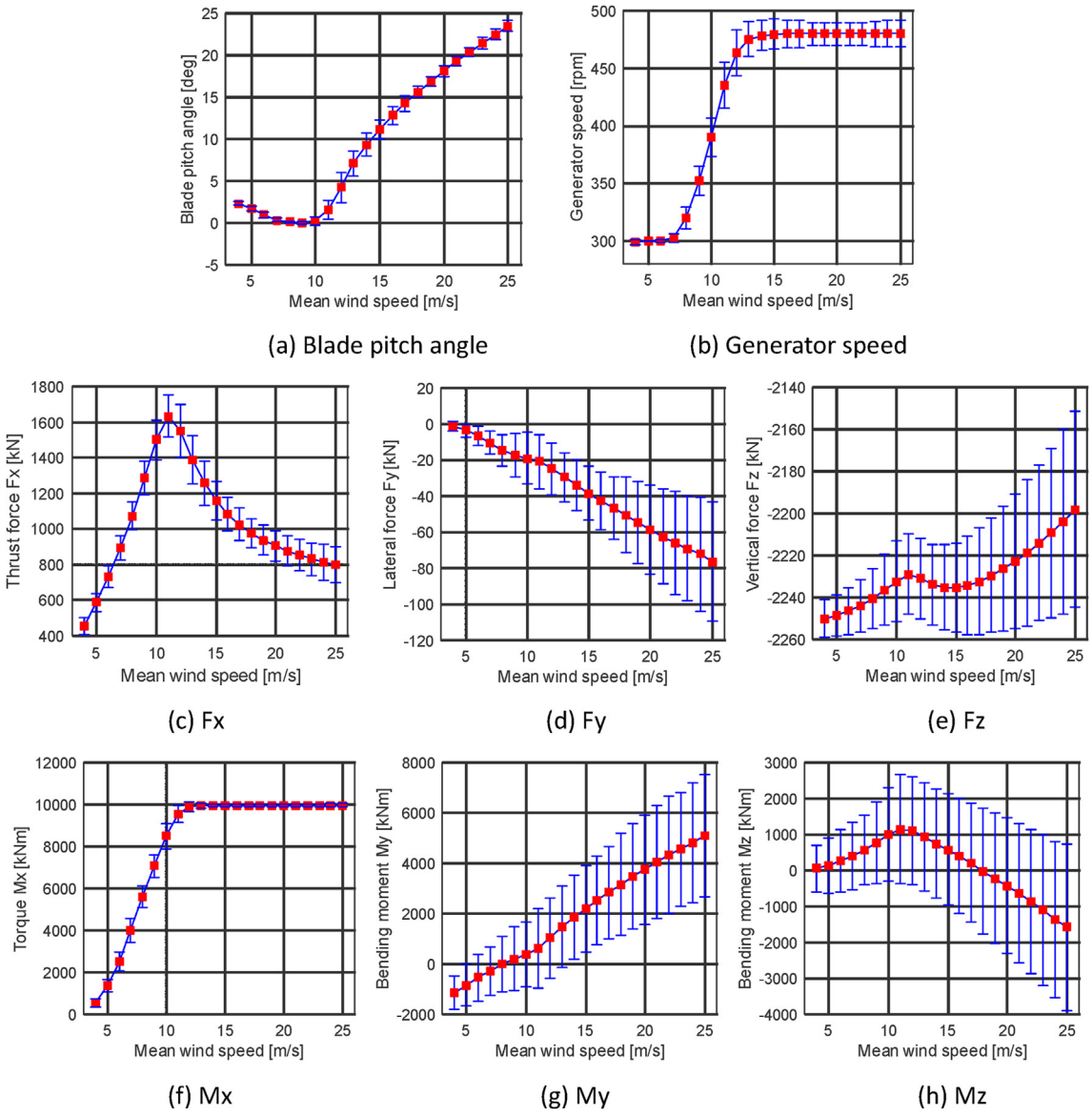

Fig. 8. Variation of performance of global responses, mean value and standard deviation of blade pitch angle, generator speed and forces and moments at hub center, with mean wind speed from cut-in to cut-out; refer to a non-rotational coordinate system at hub center (see Fig. 4 for the vector directions of the coordinate axes.).

$$\chi = \frac{D_i - D_r}{D_r} \times 100 \tag{11}$$

where D_i represents the 1-h bearing fatigue damage (averaged over 5 1-h simulations with random samples) in different mean wind speed conditions, i denotes −10%, −8%, … …, 10% difference from the reference mean wind speed. D_r represents 1-h bearing fatigue damage (averaged over 5 1-h simulations with random samples) with the reference value of mean wind speed.

Under the below-rated condition, the 1-h fatigue damage of the gearbox high-speed bearings, HS-A and HS-B is very sensitive to the variations of the mean wind speed, as shown in Table 7. In addition, the fatigue damage significantly increases as the mean wind speed increases from conditions of −10%–10% variation, corresponding to 4.5 m/s to 5.5 m/s. In contrast, small effects are observed in the fatigue damage of the main bearings and the planet carrier bearings. It is noted that percentage differences of the 1-h fatigue damage between −4 and 4 are not significant, because the statistical uncertainty might be up to 2%, as illustrated in Section 4.6 in the present work.

To explain the significant effects on the bearings HS-A and HS-B, dynamic equivalent load distributions associated with cycles of the two bearings among three mean wind speed scenarios: 10% variation, reference value (5 m/s) and 10% variation are compared, as shown in Fig. 9(a) and (b), respectively. Since the bearings HS-A and HS-B are mounted on the same shaft, an identical number of load cycles are experienced by the two bearings and there are 17931, 17938 and 17945 revolutions in 1 h under the −10% variation, reference value (5 m/s) and 10% variation conditions, respectively. The load cycles increase along with the mean wind speed because of the increase of generator speed under the below-rated condition, but this trend is not the main cause of the increasing bearing fatigue damage. As shown in the Fig. 9, mean levels of the bearing dynamic equivalent load significantly increase as the mean wind speed increases, which is the main reason for the increase of the bearing fatigue damage. The increased bearing dynamic equivalent

Table 7
Effect of variation of mean wind speed on drivetrain fatigue damage under below-rated condition.

Variation	%difference of one-hour fatigue damage					
	INP-A	INP-B	PLC-A	PLC-B	HS-A	HS-B
-10%	3.768	5.402	-1.310	-2.289	-79.682	-61.723
-8%	2.954	4.225	-1.044	-1.834	-70.655	-53.026
-6%	1.570	1.995	-0.730	-1.389	-65.149	-46.231
-4%	0.718	0.756	-0.473	-0.963	-50.670	-34.376
-2%	0.808	1.155	-0.257	-0.500	-26.399	-17.295
2%	-0.709	-0.960	0.264	0.522	33.771	20.384
4%	-2.613	-3.872	0.562	1.044	73.424	41.523
6%	-3.418	-4.979	0.826	1.653	126.220	69.309
8%	-4.101	-5.886	1.104	2.353	192.182	101.962
10%	-4.836	-6.886	1.380	3.108	273.066	139.879

Green value ($2 \leqslant |value| \leqslant 5$): slight effect. Yellow value ($5 < |value| \leqslant 10$): moderate effect. Red value ($|value| > 10$): severe effect.

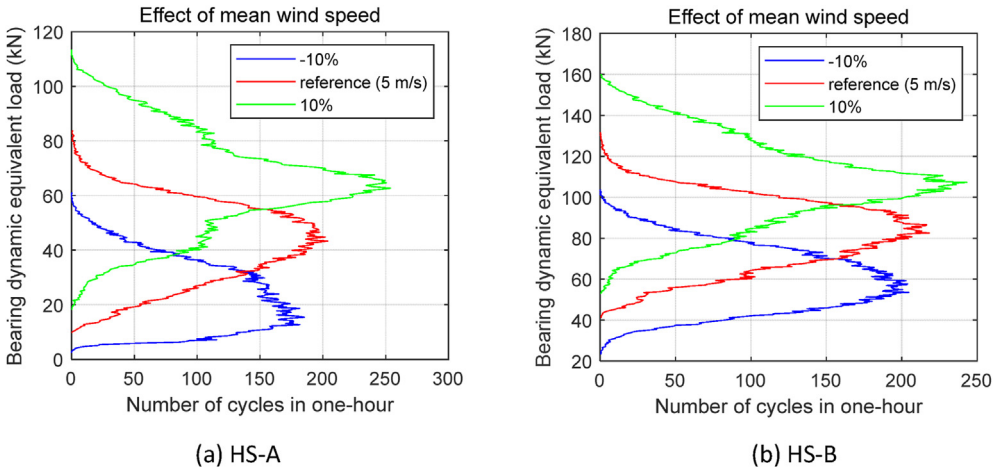

Fig. 9. Comparison of dynamic equivalent load (Eq. (7)) distribution associated with cycles (see Fig. 6.) of bearings HS-A and HS-B among three mean wind speed scenarios: 10% variation, reference value and 10% variation, under below-rated condition.

loads are caused by the increase of torque loads. From Fig. 8(f), it is observed that rotor torque evidently increases for increasing mean wind speed under the below-rated condition, which results in the increase of gear meshing force in the high-speed stage. Thus, the axial and radial forces of bearings in the high-speed shaft increase, which, according to Eq. (7), result in the increase of bearing dynamic equivalent loads.

The rated wind speed of 11.4 m/s is between the conditions of −6% (11.28 m/s) and −4% (11.52 m/s) variations from the reference value of 12 m/s. From Table 8, it is observed that near and below the rated conditions, from −10% to −6% variations in mean wind speed, significant effects generally appear in all bearings, especially for the main bearing INP-B and the high-speed bearings HS-A and HS-B. Meanwhile, above the rated condition, there is an obvious decrease in the fatigue damage of main bearings, INP-A and INP-B, as the mean wind speed increases, while small effects are observed in other bearings.

Fig. 10 compares the dynamic equivalent load distributions associated with cycles of the bearings INP-B and HS-A among three mean wind speed scenarios: 10% variation, reference value (12 m/s) and 10% variation. In Fig. 10(a), the number of load cycles experienced by the bearing INP-B in 1 h under the three mean wind speed conditions are 526, 563 and 568 revolutions, respectively. The difference in load cycles between the −10% variation and the 12 m/s conditions contributes to the difference in fatigue damage of bearings INP-A, INP-B, PLC-A and PLC-B. In addition, there is a general decrease in the mean level of bearing dynamic equivalent load from −10% to 10% variations in the mean wind speed, which is because that the increased rotor bending moment *My*, as shown in Fig. 8(g), mitigates the rotor gravity effect on the main bearings; this is another reason for the difference in the fatigue damage.

From Fig. 10(b), it is seen that the dynamic equivalent load distributions associated with cycles of the bearing HS-A in conditions of 12 m/s and 10% variation are very close, while they differ with that of the condition of −10% variation. One reason is that the load cycles in the −10% variation condition are different from those in the other conditions. After the speed increase caused by the gear ratio of 50.039, the number of load cycles experienced by the bearing HS-A in 1 h under the −10% variation, 12 m/s and 10% variation conditions are 26312, 28167 and 28430 revolutions, respectively. Another reason relates to the difference in torque loads. As discussed in the last section, the mean rotor torque and

Table 8
Effect of variation of mean wind speed on drivetrain fatigue damage under rated condition.

Variation	%difference of one-hour fatigue damage					
	INP-A	INP-B	PLC-A	PLC-B	HS-A	HS-B
-10%	8.052	14.852	-7.710	-8.117	-19.919	-18.903
-8%	8.340	15.063	-5.451	-5.443	-14.574	-13.732
-6%	6.933	11.854	-3.478	-3.214	-9.648	-9.069
-4%	4.302	7.047	-2.045	-1.717	-5.936	-5.554
-2%	2.264	3.549	-0.925	-0.536	-2.723	-2.562
2%	-2.956	-4.229	0.146	0.180	0.848	0.763
4%	-6.251	-9.445	0.114	0.236	1.455	1.264
6%	-9.619	-14.835	0.086	0.502	2.137	1.844
8%	-12.387	-19.014	0.024	0.687	2.584	2.196
10%	-15.032	-22.737	-0.095	0.842	2.824	2.387

Green value ($2 \leqslant |value| \leqslant 5$): slight effect. Yellow value ($5 < |value| \leqslant 10$): moderate effect. Red value ($|value| > 10$): severe effect.

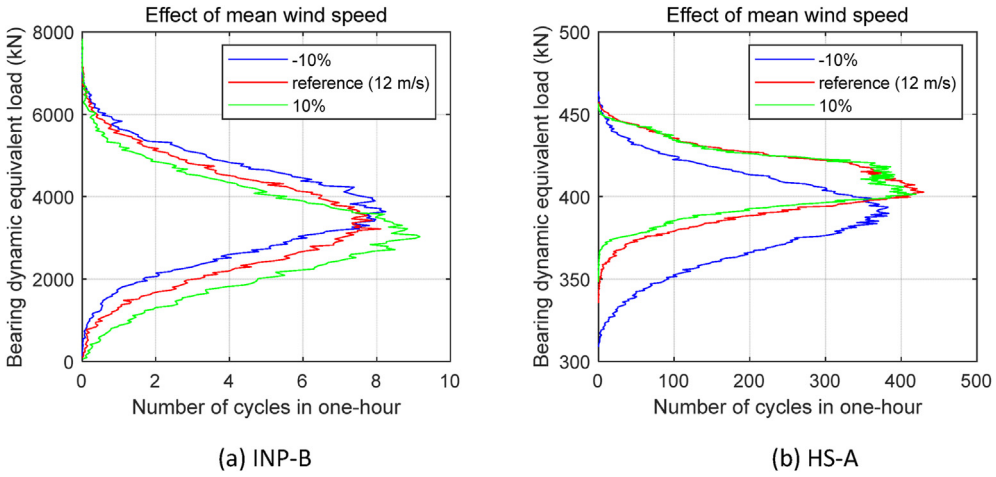

Fig. 10. Comparison of dynamic equivalent load (Eq. (7)) distribution associated with cycles (see Fig. 6.) of bearings INP-B and HS-A among three mean wind speed scenarios: 10% variation, reference value and 10% variation, under rated condition.

speed increase significantly below the rated condition, while they are almost constant after the rated condition. Therefore, fatigue damage in the high-speed bearings under the below-rated conditions is significantly smaller than that under the rated or above-rated conditions, where differences in the fatigue damage are very small.

From Table 9, it is observed that more significant effects appear for the main bearings than for other bearings under the above-rated condition. This is because fatigue damage of bearings in the gearbox is determined by load cycles and toque loads, which are constant under the above-rated condition. In contrast, fatigue damage in the main bearings is dominated by nontorque loads, specifically the bending moments *My* and *Mz*, which are very sensitive to the variation of mean wind speed, as shown in Fig. 8. It is noted that above the 6% variation conditions, if the mean wind speed exceed the cut-out value of 25 m/s for a certain duration, e.g., 5 min, the actual turbine should be shut down, but in our simulations, the operational controller keeps working since the focus of this study is on the variation of mean wind speed.

The reason for the different fatigue damage can also be revealed by Fig. 11, where dynamic equivalent load distributions associated with cycles of bearings INP-A and INP-B among three mean wind speed scenarios: 10% variation, reference value (24 m/s) and 10% variation are compared. Very similar numbers of load cycles for the two bearings are experienced in 1 h under the three conditions, and they are all about 571 revolutions. The bearing dynamic equivalent loads in the three conditions are slightly different, which are induced by the variations of the bending moments *My* and *Mz* of the drivetrain shaft, and this leads to the different fatigue damage in the main bearings.

In summary, below the rated conditions, the variation of mean wind speed significantly affect the fatigue damage in bearings in the gearbox because of the large variations of torque loads. Under the rated and above-rated conditions, fatigue damage of main bearings is sensitive to the variation of mean wind speed, which is due to the variation of rotor bending moments, while there are small effects on bearings in the gearbox. Additional attention should be paid to the near and below the rated condition, fatigue damage of all bearings in the drivetrain is sensitive to the variation of the mean wind speed in these conditions due to the large variations of rotor bending moments, torque, and load cycles. In addition, the absolute 1-h fatigue damage of bearings near the

Table 9
Effect of variation of mean wind speed on drivetrain fatigue damage under above-rated condition.

Variation	%difference of one-hour fatigue damage					
	INP-A	INP-B	PLC-A	PLC-B	HS-A	HS-B
-10%	22.794	5.737	-0.752	-0.459	-0.129	0.089
-8%	17.370	3.375	-0.580	-0.335	-0.112	0.063
-6%	12.157	1.969	-0.401	-0.243	-0.062	0.057
-4%	7.528	-1.531	-0.334	-0.195	-0.056	0.039
-2%	3.776	-0.777	-0.176	-0.119	-0.020	0.009
2%	-3.531	1.953	0.197	0.053	0.043	-0.025
4%	-6.075	5.916	0.389	0.171	0.068	-0.044
6%	-10.338	11.598	0.584	0.268	0.094	-0.069
8%	-12.509	17.880	0.797	0.355	0.110	-0.087
10%	-14.834	23.296	1.002	0.405	0.134	-0.116

Green value ($2 \leqslant |value| \leqslant 5$): slight effect. Yellow value ($5 < |value| \leqslant 10$): moderate effect. Red value ($|value| > 10$): severe effect.

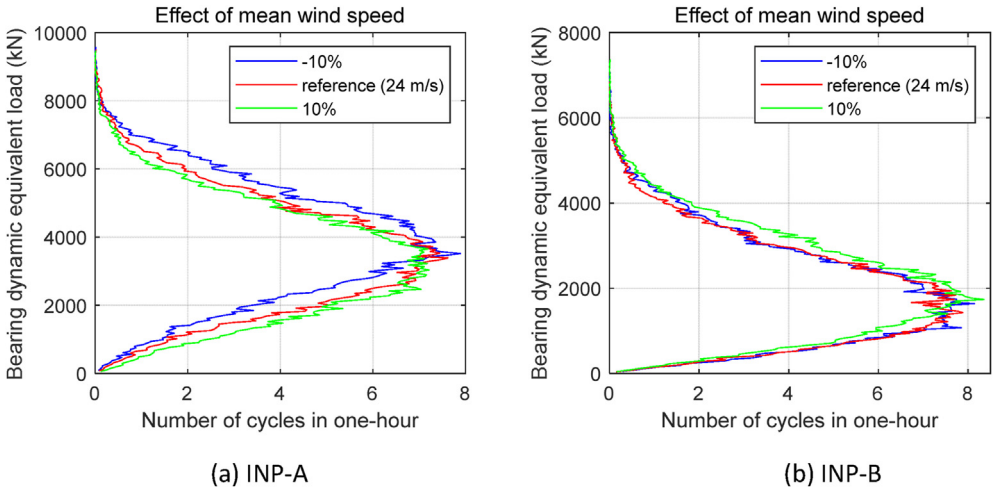

Fig. 11. Comparison of bearing dynamic equivalent load (Eq. (7)) distribution associated with cycles (see Fig. 6.) of bearings INP-A and INP-B among three mean wind speed scenarios: 10% variation, reference value and 10% variation, under above-rated condition.

rated conditions and probability of occurrence of these conditions are high, implying high contributions to the long-term fatigue damage.

Therefore, small wind speed bin sizes in the whole operating conditions are recommended, especially near and below the rated conditions, to estimate the long-term fatigue damage of drivetrain bearings.

4.2. Effect of uncertainty of the turbulence intensity

In this section, the effect of uncertainty of the turbulence intensity on drivetrain fatigue damage in different environmental conditions are studied. *TI* is an essential parameter in wind turbine design. Based on the wind turbine international standard IEC 61400-3 [18] "design requirements for offshore wind turbines", for the rotor-nacelle assembly design, wind conditions in terms of wind speed and turbulent parameters can be defined based on the IEC 61400-1 [17], where the *TI* is defined as the ratio of the standard deviation σ_1 of the turbulence and mean wind speed at hub height u_{hub}, as below [17]:

$$TI = \frac{\sigma_1}{u_{hub}} \tag{12}$$

The standard deviation σ_1 of the turbulence is calculated by Ref. [17]:

$$\sigma_1 = I_{ref}(0.75u_{hub} + b); b = 5.6\ m/s \tag{13}$$

where I_{ref} is the expected value of *TI* at 15 m/s, for wind turbine Class C, $I_{ref} = 0.12$.

According to studies of Larsen et al. [46], Chen et al. [47], Türk and Emeis [48], Myrtvedt et al. [49] and Nybø et al. [50], *TI* of wind turbines is typically related to atmospheric stability conditions and roughness lengths, and offshore conditions in the normal operating wind speed range of wind turbine are often unstable. The *TI* calculated based on the IEC 61400-3 [18] is a direct function of the mean wind speed for standard wind turbine classes, which is based on neutral atmospheric conditions and is intended to represent many different sites. These *TI* values do not give a precise representation of any specific site. Moreover, the *TI* of wind turbines

inside a wind farm would increase due to the wakes from many upwind turbines. For these reasons, *TI* is uncertain.

In the studies of Ernst and Seume [51] and Nybø et al. [52], the 90th percentile of the measured *TI* form the FINO 1, which is located in the North Sea, 45 km north of the island Borkum and near the Alpha Ventus offshore wind farm, is compared with that in the IEC 61400-3 [18]. The results show that there is an obvious deviation; in general, in low wind speed conditions, the measured results are higher than the values from the IEC standard, and the observation is opposite in intermediate and high wind speed conditions. The Alpha Ventus offshore wind farm consists of 12 5-MW wind turbines, and the study of Kretschmer et al. [53] compared the *TI* from two turbines in the wind farm with that from the FINO 1; the results show that while influenced by control and locations, *TI* measured in the wind farm is evidently higher than that in the FINO 1, especially in low wind speed conditions. Based on the comparisons from the FINO 1 and the wind farm, the variation range of the *TI* in each operating condition is considered between −10% and 10% around the reference value from the IEC 61400-3 [18] standard in this study.

Table 10 − 12 demonstrate the effect of the variation of *TI* on drivetrain 1-h fatigue damage under the below-rated, rated and above-rated operating conditions, respectively. The results are calculated based on Eq. (11) based on 5 1-h samples (see Table 11).

It is found that the variation of *TI* has a significant effect on drivetrain main bearings, INP-A and INP-B, in the three operating conditions, and severe effects are observed under the above-rated condition. Under the below-rated condition, significant effects of variation of *TI* are observed in the gearbox high-speed bearings, HS-A and HS-B. As a contrast, negligible effects of variation of *TI* are observed in the gearbox low-speed bearings, PLC-A and PLC-B, in the three operating conditions. It is noted that percentage differences of the 1-h fatigue damage between −4 and 4 are not significant, because the statistical uncertainty might up to 2%, as illustrated in Section 4.6 in the present work.

The reasons for this fact are revealed by the features of drivetrain shaft loads with variation of *TI*. Figs. 12 and 13 illustrate the effects of variation of *TI* on the mean values and standard deviations of the.

Main shaft bending moments *My* and *Mz*, respectively, at the hub center position in the three operating conditions. The coordinate system is illustrated in Fig. 5. The variation of *TI* does not lead to the change in the mean values of the main shaft bending moments, while this variation relates to the change in their standard deviations. Standard deviations of the main shaft bending moments increase with the increases of *TI* in all operating conditions, which accounts for the increases in fatigue damage of the main bearings. Fig. 14 illustrates the effect of variation of *TI* on mean values and standard deviations of the shaft torque *Mx* under the below-rated condition. It is found both the mean values and standard deviations increase with *TI*. Because the high-speed bearings carry lighter loads compared to the low- and middle-speed bearings, especially in milder environmental conditions, a slight increase in the shaft torque could result in a significant increase in fatigue damage of the high-speed bearings.

A sensitivity analysis of the main bearing fatigue damage with regards to variations in the *TI* is conducted in different operating conditions. Figs. 15–17 show the relation between the variation of *TI* and the percentage difference in the main bearing 1-h fatigue damage under the below-rated, rated and above-rated conditions, respectively. Approximately linear relations between the main bearing fatigue damage and the variation of *TI* are observed in the three operating conditions. The feature can be inferred from the comparison of bearing dynamic equivalent loads and load cycles in different *TI* conditions. Fig. 18, exemplified based on one sample, compares the bearing equivalent load distributions associated with cycles among the three *TI* scenarios: 10% variation, reference value from IEC 61400-3 [18] and 10% variation, under the above-rated condition. Load cycles in the three *TI* conditions for the two bearings are very close in 1 h, with approximately 571 revolutions. The different short-term fatigue damage is mainly caused by the different load levels in each load bin. From Eq. (10), although there is an exponential relationship between the 1-h fatigue damage *D* and the bearing dynamic equivalent load *P* due to the power exponent *a*, the small difference of *P* in different *TI* conditions makes the fatigue damage almost proportional to the variation of TI. The fitted linear equation in each figure (in Figs. 15–17 and Figs. 22–24) provides a basis for fatigue damage estimation of the main bearings of the 10 MW wind turbine drivetrain when a reasonable estimates of *TI* and wind shear are obtained from measured data in an offshore wind farm.

The sensitivity of the main bearing fatigue damage to the variation of *TI* increases as the environmental conditions become more severe. This implies that the largest effects produced by the

Table 10
Effect of variation of turbulence intensity on drivetrain fatigue damage under below-rated condition.

Variation	%difference of one-hour fatigue damage					
	INP-A	INP-B	PLC-A	PLC-B	HS-A	HS-B
-10%	-2.619	-5.226	-0.212	-0.871	-19.188	-12.204
-8%	-2.097	-4.213	-0.214	-0.674	-15.785	-9.992
-6%	-1.561	-3.168	0.004	-0.479	-12.184	-7.692
-4%	-1.017	-2.093	-0.019	-0.296	-8.434	-5.317
-2%	-0.468	-1.003	-0.037	-0.143	-4.487	-2.838
2%	0.537	1.064	0.062	0.179	4.251	2.599
4%	1.067	2.139	0.019	0.381	8.634	5.288
6%	1.623	3.262	0.062	0.526	13.238	8.090
8%	2.192	4.410	0.086	0.799	17.870	10.923
10%	2.731	5.497	0.355	1.004	22.718	13.811

Green value ($2 \leqslant |value| \leqslant 5$): slight effect. Yellow value ($5 < |value| \leqslant 10$): moderate effect. Red value ($|value| > 10$): severe effect.

Table 11
Effect of variation of turbulence intensity on drivetrain fatigue damage under rated condition.

Variation	%difference of one-hour fatigue damage					
	INP-A	INP-B	PLC-A	PLC-B	HS-A	HS-B
-10%	-7.798	-14.464	0.496	0.724	1.343	1.286
-8%	-6.204	-11.499	0.394	0.651	1.067	1.013
-6%	-4.766	-8.812	0.304	0.417	0.830	0.760
-4%	-3.027	-5.769	0.186	0.246	0.503	0.445
-2%	-1.806	-3.454	0.068	0.122	0.230	0.170
2%	1.492	2.776	-0.056	-0.034	-0.110	-0.173
4%	3.175	5.898	-0.197	-0.199	-0.394	-0.437
6%	4.986	9.345	-0.246	-0.262	-0.600	-0.603
8%	6.629	12.548	-0.336	-0.404	-0.844	-0.842
10%	8.039	15.348	-0.438	-0.553	-1.085	-1.125

Green value ($2 \leqslant |value| \leqslant 5$): slight effect. Yellow value ($5 < |value| \leqslant 10$): moderate effect. Red value ($|value| > 10$): severe effect.

Table 12
Effect of variation of turbulence intensity on drivetrain fatigue damage under above-rated condition.

Variation	%difference of one-hour fatigue damage					
	INP-A	INP-B	PLC-A	PLC-B	HS-A	HS-B
-10%	-18.778	-26.829	-0.146	-0.063	-0.041	-0.016
-8%	-15.231	-21.861	-0.115	-0.007	-0.013	-0.020
-6%	-11.724	-16.940	-0.088	-0.031	-0.045	-0.003
-4%	-7.978	-11.570	-0.071	-0.019	-0.041	-0.021
-2%	-4.135	-6.081	-0.039	-0.021	0.026	0.006
2%	4.268	6.263	0.030	0.008	-0.003	-0.004
4%	8.388	12.441	0.095	0.007	-0.006	-0.011
6%	12.831	19.162	0.130	0.023	0.013	0.008
8%	17.168	25.751	0.182	0.044	0.013	0.019
10%	21.933	32.952	0.182	0.071	0.004	0.018

Green value ($2 \leqslant |value| \leqslant 5$): slight effect. Yellow value ($5 < |value| \leqslant 10$): moderate effect. Red value ($|value| > 10$): severe effect.

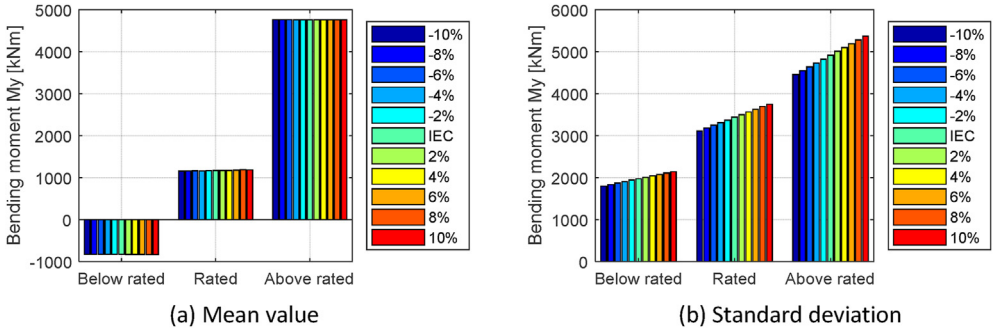

Fig. 12. Effect of variation of turbulence intensity on mean values and standard deviations of bending moment *My* at the hub center under below-rated, rated and above-rated conditions.

variations of *TI* should be observed under the above-rated conditions. The sensitivity in the certain *TI* variation range provides a basis for estimation of the actual fatigue damage effect when actual measurements of the *TI* uncertainty are available.

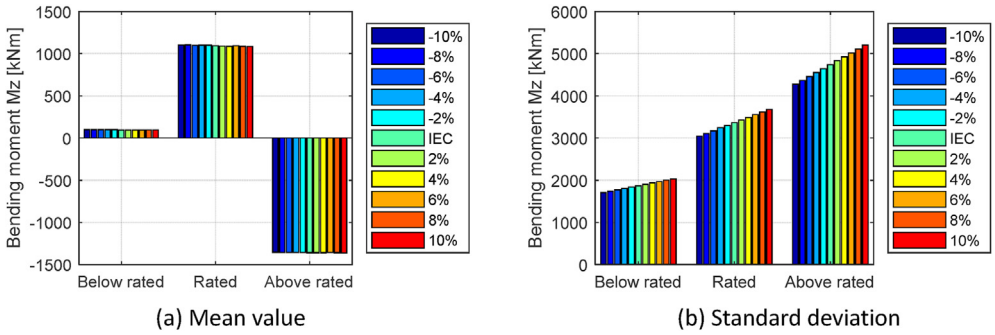

Fig. 13. Effect of variation of turbulence intensity on mean values and standard deviations of bending moment *Mz* at the hub center under below-rated, rated and above-rated conditions.

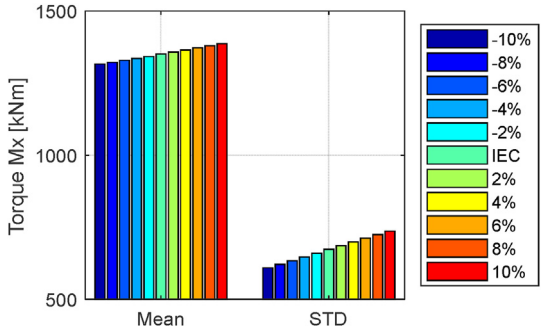

Fig. 14. Effect of variation of turbulence intensity on mean values and standard deviations of Torque *Mx* at hub center under below-rated condition.

4.3. Effect of uncertainty of the wind shear

Wind shear refers to the variation of mean wind speed with height above the still water level. The wind speed vertical gradient would lead to inconsistent aerodynamic loads acting on the blades at different positions, which directly affects the dynamic response of wind turbine drivetrains. Therefore, investigating the effect of wind speed vertical gradient on drivetrain performance is important. Two formulations are commonly used to model the wind speed profile: the power law and the logarithm law [54]. In this study, the power law is used to describe the wind speed profile as below [18]:

$$u(z) = u_{hub}(z/z_{hub})^{\alpha} \tag{14}$$

where $u(z)$ represents the mean wind speed at the height z above the still water level, u_{hub} denotes the reference value of the mean wind speed at the hub height, z_{hub} represents the hub height above the still water level. α is the power law exponent, which is recommended in IEC 61400-3 [18] to be 0.14 for offshore locations.

However, the reference value of the power law exponent from the IEC standard is uncertain. Tuerk et al. [55] investigate the wind profile above the sea based on four years of FINO1 data from September 2003 to August 2007; the results show that at the location of FINO1, the mean value of the power law exponent is 0.10, but it has a large variation and strongly depends on wind speed and atmospheric stability. The mean value of the power law exponent generally increases with the wind speed and it varies approximately from 0.10 to 0.14 in the wind speed range of 8–20 m/s and remains nearly constant 0.13 when the wind speed increases further. However, a larger variation is seen due to the different atmospheric stability classes, and it reaches a maximum of 0.19 under very stable conditions.

In this work, a reference variation range of the power law exponent between −10% and 10% around the reference value 0.14 from the IEC 61400-3 [18] standard is considered in each operating condition to carried out sensitivity study. The actual effect on drivetrain fatigue damage can be estimated with the actual measure of the uncertainty of the power law exponent based on the sensitivities.

Fig. 19 compares the mean wind speed profiles for a given mean

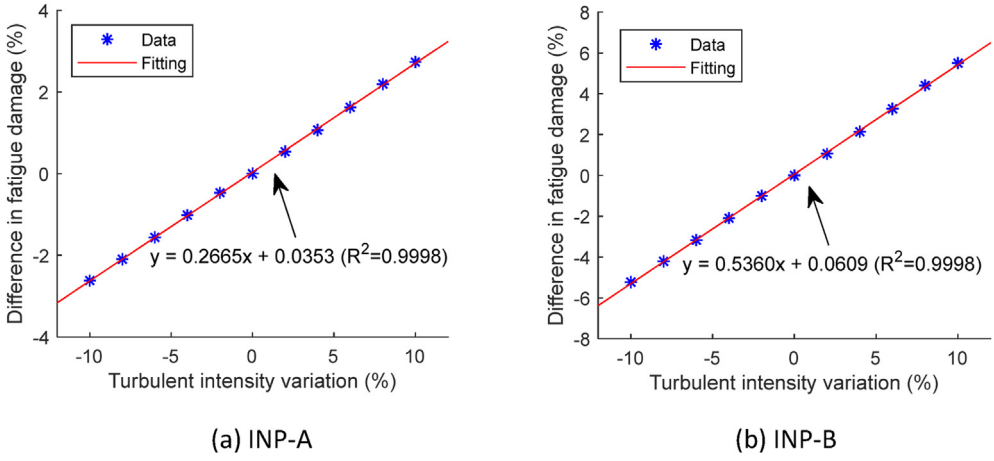

Fig. 15. Relations between turbulence intensity variation and percentage difference in 1-h fatigue damage of drivetrain main bearings under below-rated condition.

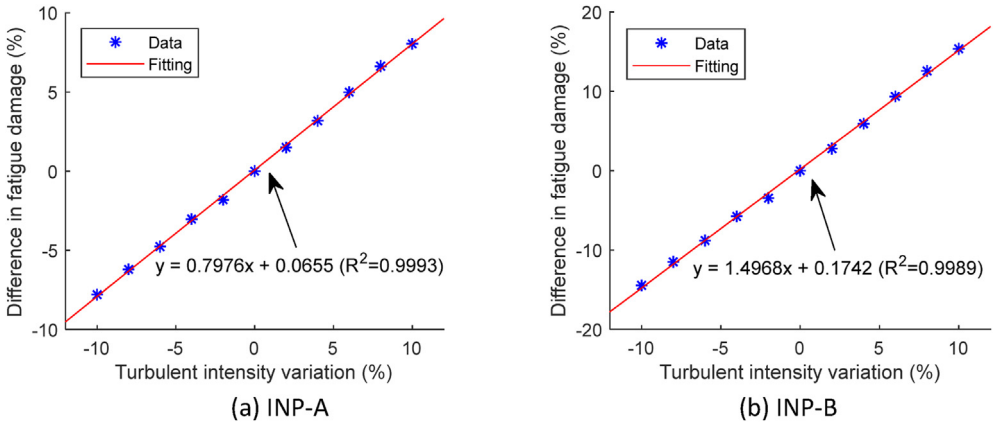

Fig. 16. Relations between turbulence intensity variation and percentage difference in 1-h fatigue damage of drivetrain main bearings under rated condition.

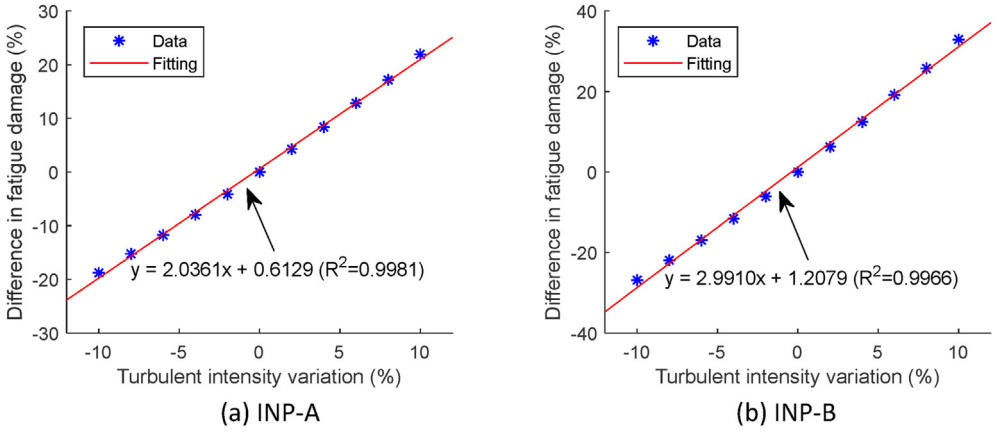

Fig. 17. Relations between turbulence intensity variation and percentage difference in 1-h fatigue damage of drivetrain main bearings under above-rated condition.

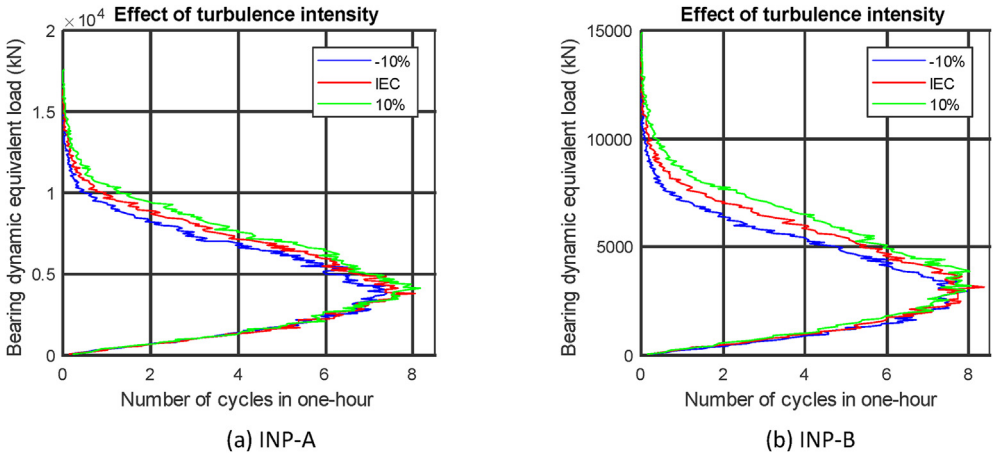

Fig. 18. Comparison of bearing dynamic equivalent load (Eq. (7)) distribution associated with cycles (see Fig. 6.) among three turbulence intensity scenarios: 10% variation, reference value and 10% variation, under above-rated condition.

wind speed at the hub height and variable exponent α under the below-rated, rated and above-rated conditions. It is shown that the mean wind speed varies more with the height if a greater power law exponent is applied, which would lead to greater rotor load imbalance. Therefore, the nontorque bending moments at the hub center are expected to differ when different power law exponents are applied (see Table 12).

Figs. 20 and 21 demonstrate the effects of variation of wind shear on the mean values and standard deviations of the bending moments *My* and *Mz* at hub center in the three operating conditions. It is shown that the mean values of the bending moments increase along with the power law exponent, while the standard

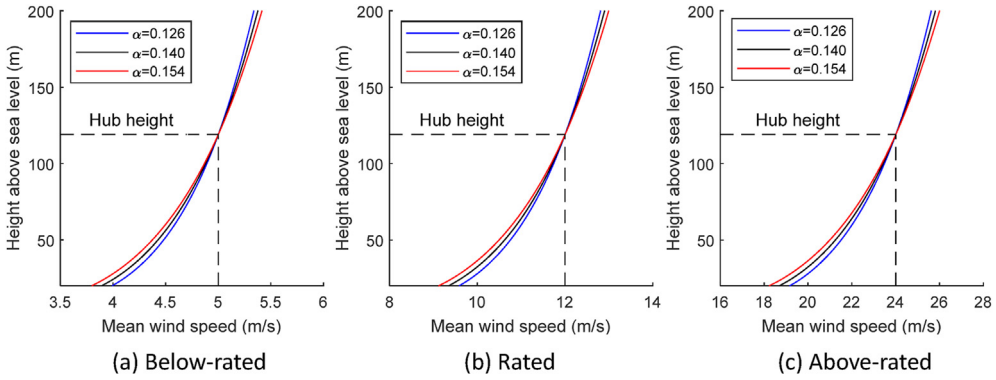

Fig. 19. Comparison of mean wind speed profiles in three wind shear scenarios: 10% variation ($\alpha = 0.126$). reference value ($\alpha = 0.140$) and 10% variation ($\alpha = 0.154$), under below-rated, rated and above-rated conditions.

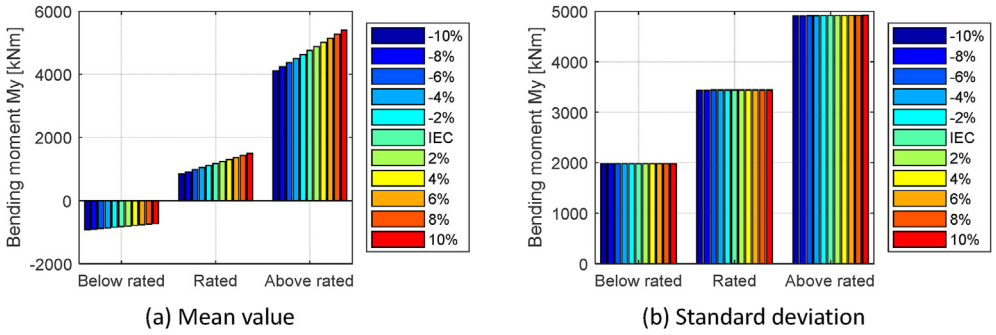

Fig. 20. Effect of variation of wind shear on mean values and standard deviations of bending moment My at hub center under below-rated, rated and above-rated conditions.

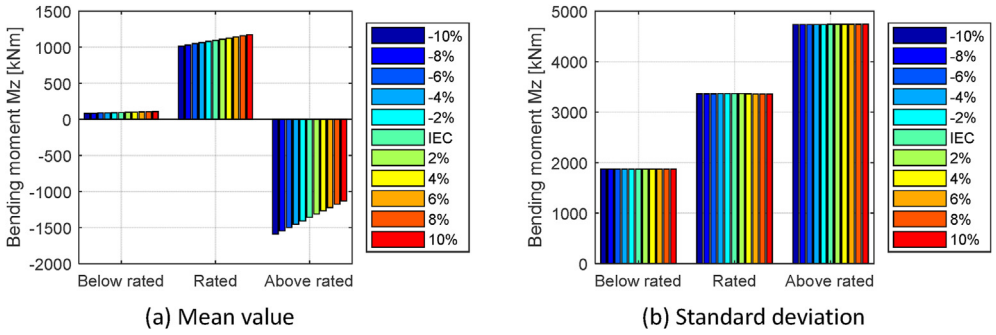

Fig. 21. Effect of variation of wind shear on mean values and standard deviations of bending moment Mz at hub center under below-rated, rated and above-rated conditions.

deviations almost remain constant. Table 13 – 15 demonstrate the effect of variation of wind shear on the 1-h fatigue damage under the below-rated, rated and above-rated conditions, respectively. The results are calculated based on Eq. (11) based on 5 1-h samples. The percentage differences of the 1-h fatigue damage between −4 and 4 are not important due to the effect caused by the statistical uncertainty. Significant effects are observed on the main bearing fatigue damage, while there is no obvious effect on fatigue damage of the bearings in the gearbox. In addition, more appreciable effects are generally found in more severe environmental conditions (see Table 14).

The sensitivity analysis of the main bearing fatigue damage to variation of wind shear exponent is conducted in different environmental conditions. Figs. 22–24 illustrate relations between the variation of the wind shear exponent and the percentage difference in the 1-h fatigue damage of the main bearings under the below-rated, rated and above-rated conditions, respectively. Different from the trend of the variation of *TI*, the percentage difference in the fatigue damage of main bearings decreases when the variation of the wind shear exponent increases. This is because the rotor pitch bending moment mitigates the rotor gravity effects on fatigue damage of the main bearings.

The 1-h fatigue damage of main bearings approximately decreases linearly as the variation of wind shear exponent increases. The reason is same with that analyzed in Section 4.2, i.e., the small difference of bearing dynamic equivalent loads in different wind shear conditions renders the fatigue damage vary almost proportionally; the variation is not caused by load cycles, because as illustrated in Fig. 25, the load cycles in the three wind shear conditions are very similar with about 571 revolutions in 1 h. The gradients of the lines are larger in more severe environmental conditions than they are in the milder conditions, implying the

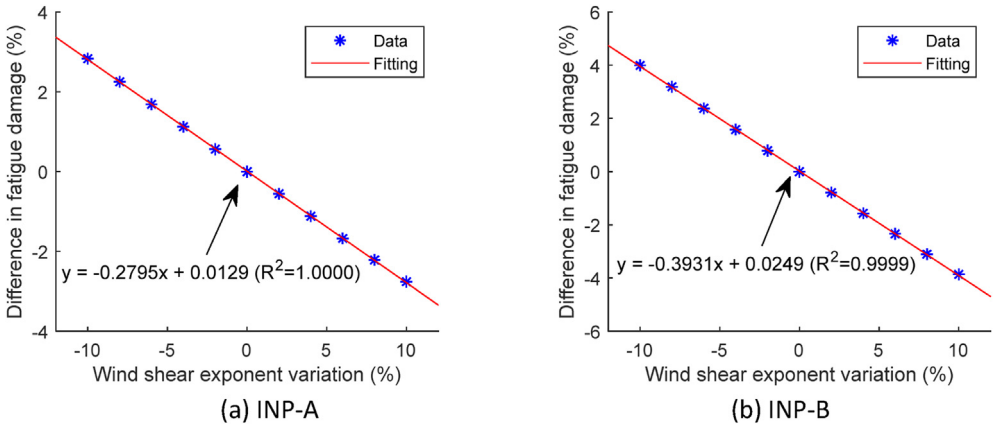

Fig. 22. Relations between wind shear exponent variation and percentage difference in fatigue damage of drivetrain main bearings under below-rated condition.

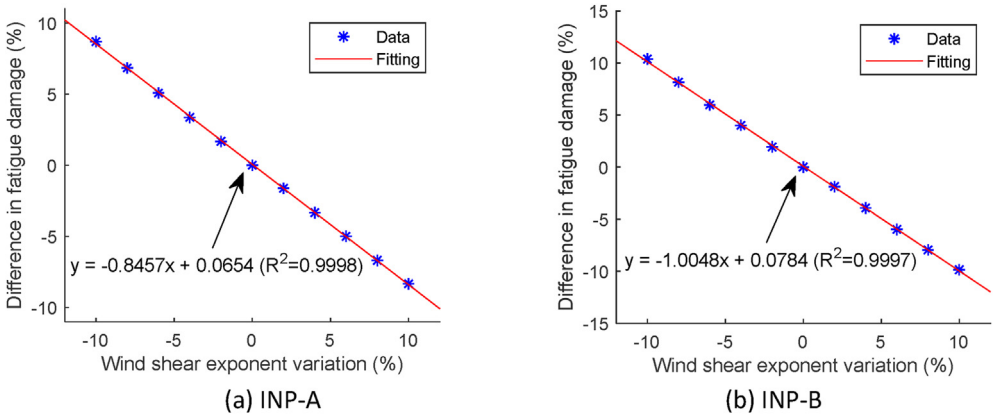

Fig. 23. Relations between wind shear exponent variation and percentage difference in fatigue damage of drivetrain main bearings under rated condition.

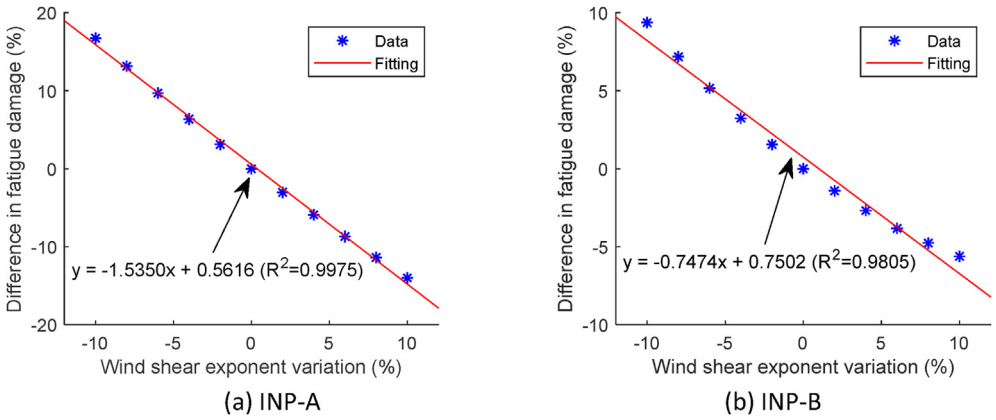

Fig. 24. Relations between wind shear exponent variation and percentage difference in fatigue damage of drivetrain main bearings under above-rated condition.

increased sensitivity of the fatigue damage to the wind shear exponent.

4.4. Effect of variability and uncertainty of the significant wave height and wave spectral peak period

Irregular waves have a random nature, varying in wave height, wave period, and the main propagation direction. A sea state is generally characterized by the significant wave height, H_s and the spectral peak period, T_p. The sea state at a given site may consists of a swell with a relatively long period (>10 s) and a locally generated wind sea with a relatively short period. In this study, only the local wind sea is considered which is affected by local site conditions such as mean wind speed, fetch, water depth and bathymetry [18]. The effect of the fundamental variability of significant wave height and spectral peak period on the 10-MW drivetrain short-term fatigue damage are studied in this section.

Figs. 26 and 27 show the conditional distributions of significant

Table 13
Effect of variation of wind shear on drivetrain fatigue damage under below-rated condition.

Variation	%difference of one-hour fatigue damage					
	INP-A	INP-B	PLC-A	PLC-B	HS-A	HS-B
-10%	2.831	3.996	-0.235	-0.137	0.348	0.425
-8%	2.253	3.192	-0.244	-0.103	0.256	0.325
-6%	1.687	2.375	-0.038	-0.092	0.193	0.252
-4%	1.124	1.580	-0.101	-0.070	0.124	0.141
-2%	0.563	0.790	-0.021	-0.045	0.063	0.073
2%	-0.554	-0.788	-0.036	0.033	-0.068	-0.087
4%	-1.115	-1.569	0.010	0.061	-0.081	-0.168
6%	-1.673	-2.339	0.044	0.093	-0.117	-0.238
8%	-2.214	-3.102	0.057	0.118	-0.214	-0.309
10%	-2.760	-3.863	0.090	0.152	-0.201	-0.380

Green value ($2 \leqslant |\text{value}| \leqslant 5$): slight effect.

Table 14
Effect of variation of wind shear on drivetrain fatigue damage under rated condition.

Variation	%difference of one-hour fatigue damage					
	INP-A	INP-B	PLC-A	PLC-B	HS-A	HS-B
-10%	8.689	10.378	-0.517	-0.218	0.149	0.162
-8%	6.838	8.148	-0.422	-0.192	0.076	0.126
-6%	5.079	5.972	-0.322	-0.140	0.080	0.084
-4%	3.372	4.009	-0.209	-0.107	0.081	0.043
-2%	1.681	1.934	-0.102	-0.049	0.050	0.067
2%	-1.618	-1.880	0.109	0.026	0.001	-0.044
4%	-3.327	-3.926	0.204	0.094	0.015	-0.069
6%	-4.986	-5.975	0.345	0.231	0.029	-0.068
8%	-6.681	-7.949	0.467	0.282	0.047	-0.076
10%	-8.327	-9.849	0.576	0.324	0.059	-0.058

Green value ($2 \leqslant |\text{value}| \leqslant 5$): slight effect. Yellow value ($5 < |\text{value}| \leqslant 10$): moderate effect. Red value ($|\text{value}| > 10$): severe effect.

wave height for given three mean wind speed conditions and spectral peak period for given three significant wave heights, respectively. In each PDF, the 25% quantile, most probable and 75% quantile values are selected, which are marked in Figs. 26 and 27 to compare the corresponding drivetrain fatigue damage. Only one variable is changed when conducting the comparative analysis, with the other variable fixed as the most probable value.

Figs. 28 and 29 compare the 1-h fatigue damage based on 5 1-h samples in different significant wave heights and spectral peak periods, respectively, under the below-rated, rated and above-rated wind speed conditions. The comparisons are expressed by the ratio of 1-h fatigue damage between the 25% or the 75% condition and the most probable condition. As the fatigue damage in the most probable H_s or T_p conditions are used as the baseline, the ratio of fatigue damage has unit value in the figures. A slight increase in the fatigue damage of main bearings is observed as the H_s increases under the rated and above-rated wind speed conditions, while no obvious change is seen in the fatigue damage of main bearings due to the variation of T_p under given wind speed and significant wave height conditions.

Fig. 30 compares the mean values and standard deviations of the main bearing radial forces based on 5 1-h samples, which are the main cause to the fatigue damage in the three H_s scenarios under the rated wind speed condition. It is found that the standard deviations of the vertical force F_z of the two main bearings increase as the H_s increases, while other response statistics remain almost constant to the variation of the H_s. This means that the slight increase, as shown in Fig. 28, in fatigue damage is caused by the increase of the standard deviations of vertical force F_z of the two main bearings. Fig. 31 compares the power spectra of the vertical force F_z of the main bearings in the three H_s scenarios under the rated wind speed condition. It is found that even though the low frequency responses induced by turbulent wind are dominating, the main variations in the spectra are due to the responses induced by wave forces which increase as H_s increases.

The most likely cause of the change in the vertical force F_z of the main bearings is the change of global vertical force and pitch bending moment at the hub center. Fig. 32 compares the power spectra of the two global loads in the three H_s scenarios under the rated wind speed condition. It is seen that even though wave

Table 15
Effect of variation of wind shear on drivetrain fatigue damage under above-rated condition.

Variation	%difference of one-hour fatigue damage					
	INP-A	INP-B	PLC-A	PLC-B	HS-A	HS-B
-10%	16.752	9.365	-1.042	-0.672	-0.112	0.102
-8%	13.165	7.185	-0.809	-0.528	-0.078	0.095
-6%	9.708	5.166	-0.592	-0.422	-0.072	0.070
-4%	6.367	3.247	-0.391	-0.232	-0.066	0.042
-2%	3.134	1.559	-0.185	-0.111	-0.032	0.011
2%	-3.004	-1.411	0.226	0.166	0.007	-0.032
4%	-5.895	-2.677	0.439	0.289	0.022	-0.057
6%	-8.690	-3.814	0.646	0.414	0.031	-0.100
8%	-11.375	-4.756	0.877	0.579	0.062	-0.117
10%	-13.984	-5.614	1.072	0.673	0.070	-0.139

Green value ($2 \leqslant |value| \leqslant 5$): slight effect. Yellow value ($5 < |value| \leqslant 10$): moderate effect. Red value ($|value| > 10$): severe effect.

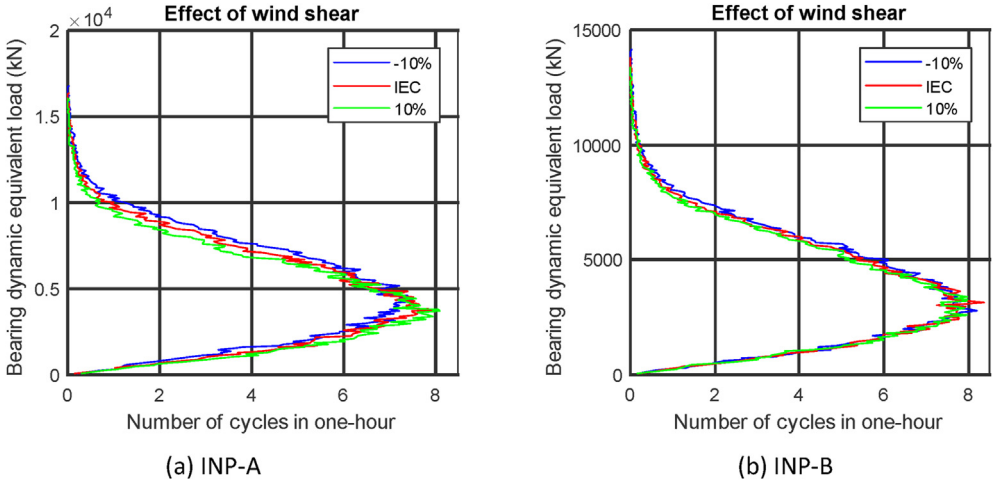

Fig. 25. Comparison of bearing dynamic equivalent load (Eq. (7)) distribution associated with cycles (see Fig. 6.) among three wind shear scenarios: 10% variation, reference value and 10% variation, under above-rated condition.

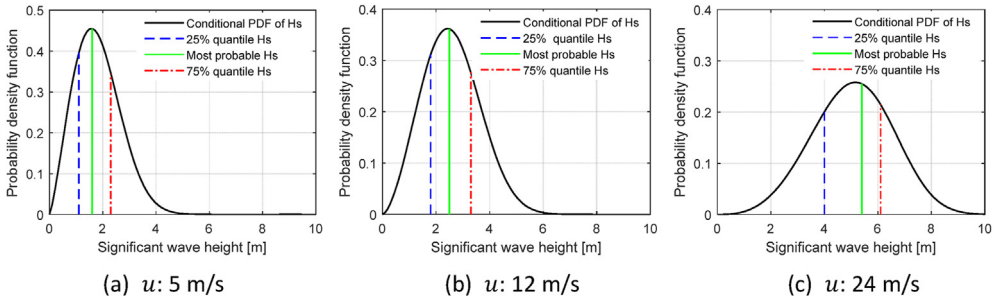

Fig. 26. Conditional distributions of significant wave height H_s for given mean wind speeds of 5 m/s, 12 m/s and 24 m/s at hub height, respectively.

frequency response, in the global vertical force spectra, increases significantly as the H_s increases, the magnitude of the force is much smaller than that of the platform pitch-induced bending moment. In addition, the power spectra of the global pitch bending moment is demonstrated in the same manner as that of vertical force of main bearings, as shown in Fig. 31. Thus, it can be inferred that the variation of global pitch bending moment leads to the change of vertical force, and consequently results in the slight increase in fatigue damage of the main bearings.

The variation of global pitch bending moment is mainly induced by variation of inertia force in the platform pitch direction. This can be revealed from the Fig. 33, where comparison of the power

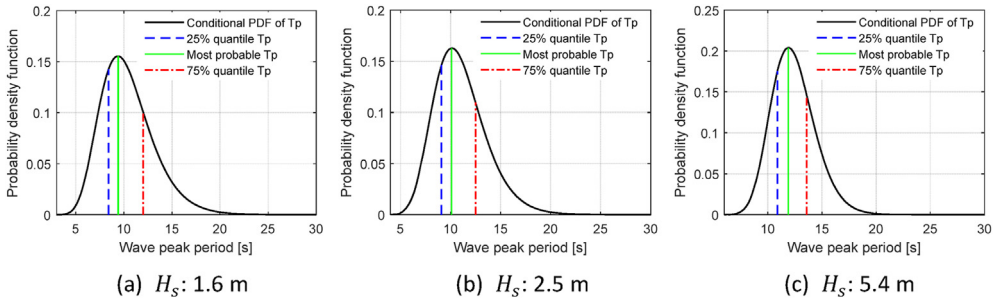

Fig. 27. Conditional distributions of wave peak period T_p for given significant wave heights of 1.6 m, 2.5 m and 5.4m, respectively.

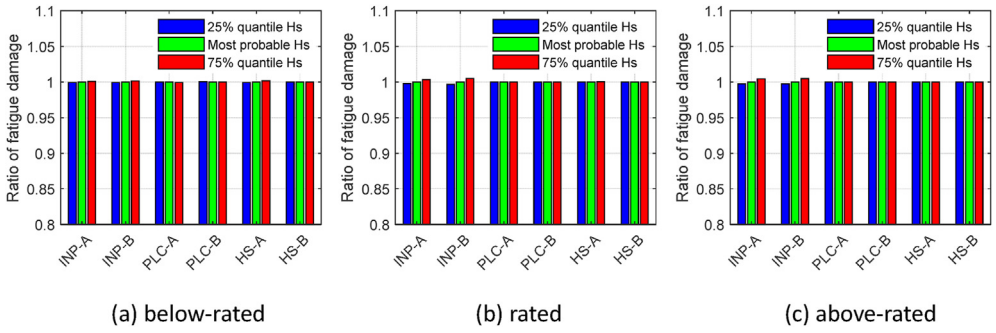

Fig. 28. Comparison of drivetrain 1-h fatigue damage in different significant wave heights H_s under below-rated, rated and above-rated wind speed conditions.

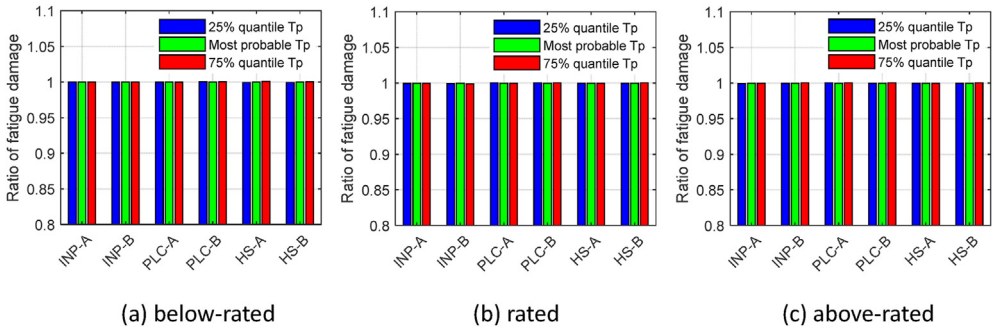

Fig. 29. Comparison of drivetrain 1-h fatigue damage in different spectral peak periods T_p under below-rated, rated and above-rated wind speed conditions.

spectra of the nacelle pitch acceleration in the three H_s scenarios under the rated wind speed condition is illustrated. It is observed that both the pitch resonant response and the wave frequency response are dominating in the power spectra and the response induced by platform pitch resonance does not change with the increase of the H_s. In contrast, the wave frequency response in the power spectra increases significantly as the H_s increases, since wave forces acting on the platform increase.

Because the natural frequencies of this wind turbine system, as shown in Table 3, and the wave excitation frequency, as shown in Table 5, are quite far apart, the platform motions are not sensitive to the variation of the T_p in a small range for given u and H_s, and hence the global loads do not vary much. Fig. 34 compares the power spectra of the nacelle pitch acceleration and pitch bending moment at hub center in the three T_p scenarios under the rated wind speed condition. It is seen even though the wave frequency response is dominating in the power spectra of nacelle pitch acceleration, it is much less sensitive to the variation of T_p compared to the variation of the H_s, as illustrated in Fig. 33. In addition, in the power spectra of the global pitch bending moment, no obvious change is observed in the wave frequency response as T_p increases, which accounts for the results of the unchanged fatigue damage of main bearing, as seen in Fig. 29.

4.5. Effect of uncertainty of the wind and wave misalignment

The directions of wind and waves can be significantly misaligned in all atmospheric conditions [56,57]. In general, small misalignments appear at all wind speeds and large misalignment occur at lower wind speeds [58]. However, IEC 61400-3 [18] indicates that for calculation of the loads acting on RNA, wind and waves can generally be assumed to be always colinear and that both the wind and waves act in a single direction.

In this section, effect of wind-wave misalignment on drivetrain fatigue damage are studied. Four wind-wave misalignment conditions, a 0-degree wind direction ($\beta_{wind} = 0°$) with four wave directions ($\beta_{wave} = 0°, 30°, 60°, 90°$) are considered, as illustrated in Fig. 35.

Nacelle motion velocities of FWTs have important influences on the drivetrain dynamic response because these velocities lead to

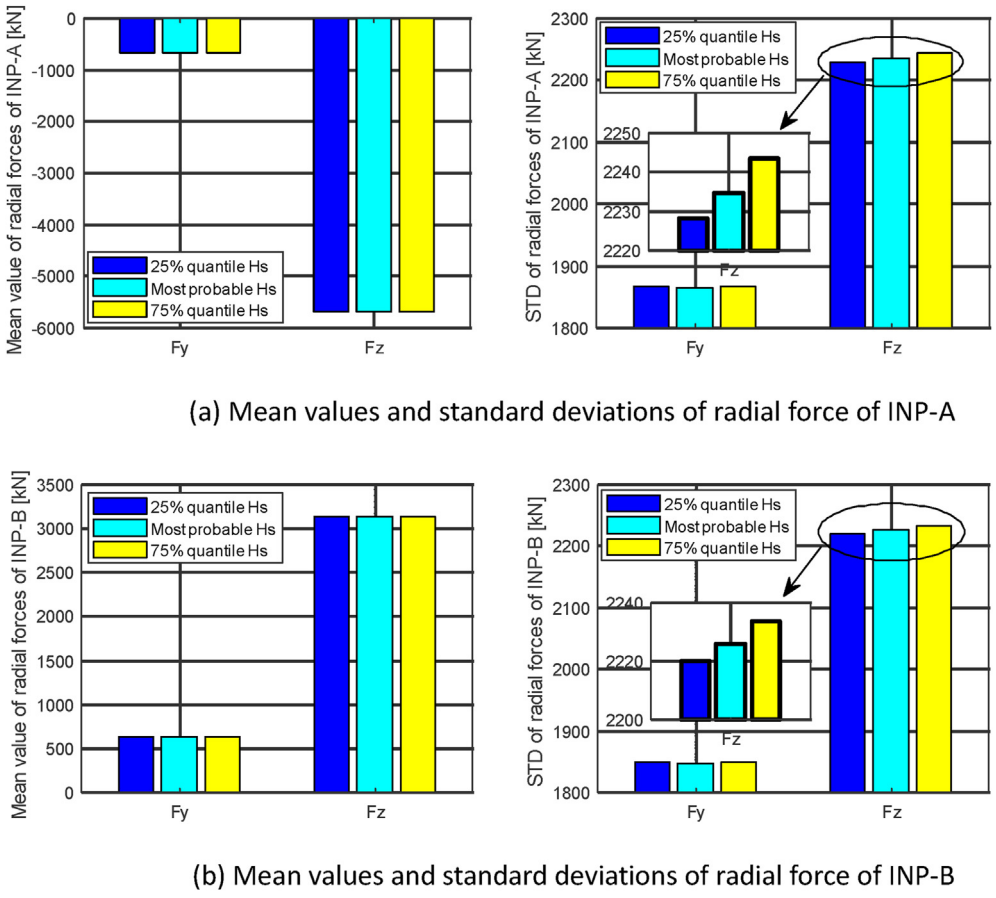

Fig. 30. Comparison of mean values and standard deviations of radial forces of main bearings INP-A and INP-B in different significant wave heights H_s under rated wind speed condition.

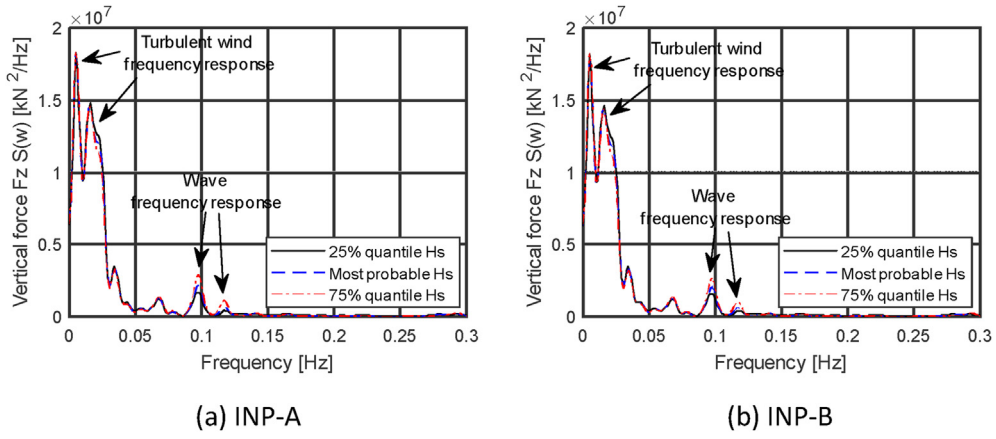

Fig. 31. Comparison of power spectra of vertical force F_z of main bearings INP-A and INP-B in different significant wave heights H_s under rated wind speed condition.

changes in the induced velocity of the air flow, thereby resulting in the aerodynamic load changes. Fig. 36 compares the time- and frequency-domain results of the nacelle surge, pitch and yaw velocities under different wind-wave misalignment scenarios for the above-rated condition. It is seen that fluctuations of surge and pitch velocities decrease with increasing β_{wave}. The main reason is revealed in the power spectra, where it is shown an increase in the pitch resonant response and a decrease in the wave frequency response. The main contribution to the decrease of fluctuations of surge and pitch velocities is determined by the decreased wave frequency response for increasing β_{wave}. The increase in the pitch resonant response with increasing β_{wave} is due to the decrease in the aerodynamic damping, which relates to the fore-aft motion of the nacelle and is less effective when the waves come from different directions from the wind direction.

In the time series of the nacelle yaw velocity, larger fluctuations are observed for $\beta_{wave} = 30\ deg$ and $\beta_{wave} = 90\ deg$ than for $\beta_{wave} = 0\ deg$ and $\beta_{wave} = 60\ deg$. This observation can be explained by the

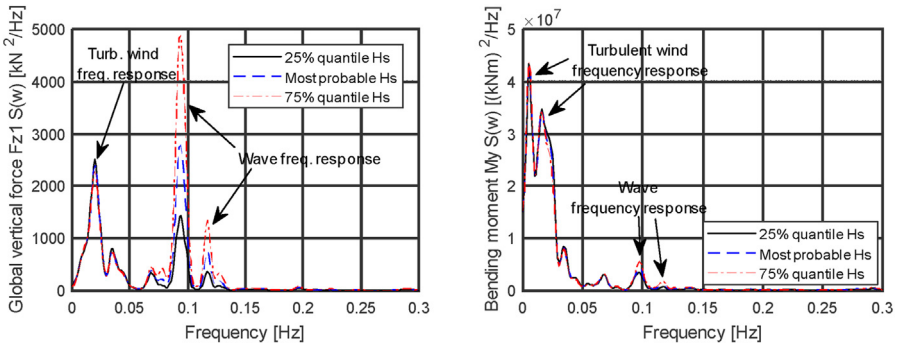

(a) Global vertical force F_{z1} at hub center (b) Global bending moment M_y at hub center

Fig. 32. Comparison of vertical force F_{z1} and bending moment M_y of global responses at the hub center in different significant wave heights H_s under rated wind speed condition.

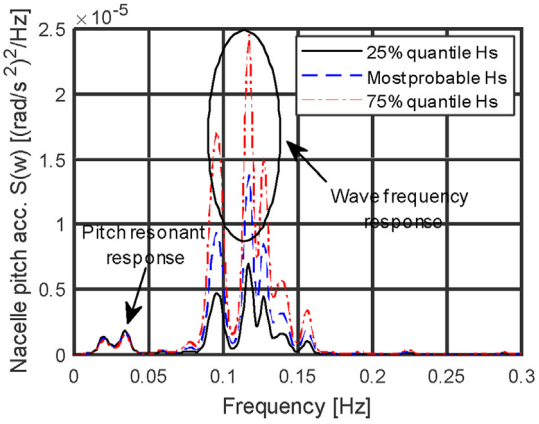

Fig. 33. Comparison of power spectra of nacelle pitch acceleration in different significant wave heights H_s under rated wind speed condition.

wave frequency responses, as illustrated in the power spectra. Based on the shape of the axially symmetrical floating substructure, two columns experience wave forces with the same phase angle compared to the incoming wave when it comes from 0 deg to 60 deg, while the phase angles are different when the wave comes from 30 deg or 90 deg. Therefore, the wave forces applied on the columns are symmetrical for $\beta_{wave} = 0\,deg$ and $\beta_{wave} = 60\,deg$, while they are asymmetrical for $\beta_{wave} = 30\,deg$ and $\beta_{wave} = 90\,deg$. This difference results in the larger response of yaw motions for $\beta_{wave} = 30\,deg$ and $\beta_{wave} = 90\,deg$. The nacelle yaw motion will affect the induced velocity at different azimuth positions of rotor plane, which renders the bending moments at the drivetrain shaft larger, thereby increasing the load effects of the drivetrain.

Fig. 37 compares the drivetrain 1-h fatigue damage based on 5 simulations with random samples for 0 deg, 30 deg, 60 deg and 90 deg wind-wave misalignments under the below-rated, rated and above-rated operating conditions, respectively. The comparisons are expressed via ratio of 1-h fatigue damage between the condition $\beta_{wave} = 30\,deg$, $\beta_{wave} = 60\,deg$ or $\beta_{wave} = 90\,deg$ and the condition $\beta_{wave} = 0\,deg$. In general, very close fatigue damage of drivetrain bearings is observed in different wind-wave misalignment cases in the wind turbine operating conditions.

Nevertheless, in the below-rated environmental condition, the fatigue damage in the gearbox's high-speed bearings, HS-A and HS-B, tends to increase slightly with increasing β_{wave}. This is because the nacelle roll motion increases with increasing β_{wave}, then the increased inertia forces of the high-speed shaft lead to increases in the bearing equivalent dynamic load, resulting in a further increase in the bearing fatigue damage. In the rated and above-rated environmental conditions, the effect of wind-wave misalignment is shown on the main bearings, while there is almost no effect on bearings in the gearbox. Greater effects are observed in the above-rated environmental condition than in the rated condition because of the more severe sea states associated. The largest fatigue damage of the main bearings is observed for $\beta_{wave} = 30\,deg$, while the smallest value is reported for $\beta_{wave} = 60\,deg$. This is because the

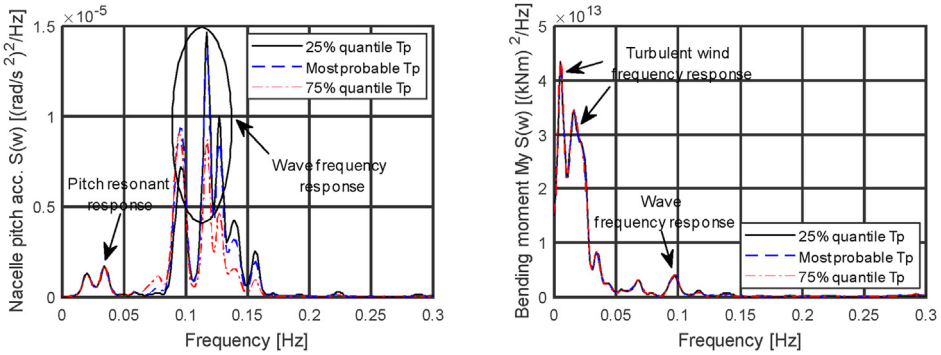

(a) nacelle pitch acceleration (b) Global bending moment M_y at hub center

Fig. 34. Comparison of power spectra of nacelle pitch acceleration and global bending moment M_y at hub center in different spectral peak period T_p under rated wind speed condition.

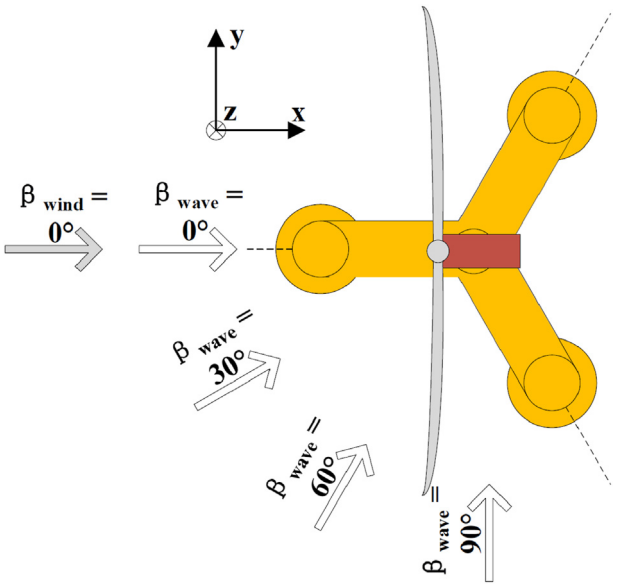

Fig. 35. Top view of wind-wave misalignment conditions.

largest variation of aerodynamic loads is produced for $\beta_{wave} = 30$ *deg*, while the smallest one is generated for $\beta_{wave} = 60$ *deg*. The reason for this is that when $\beta_{wave} = 30$ *deg*, variations of the nacelle surge, pitch and yaw velocities are all significantly induced by wave forces, while in the condition $\beta_{wave} = 60$ *deg*, variations of nacelle surge and pitch velocities are slightly induced and yaw velocity is not induced by wave forces.

4.6. Effect of uncertainty of the number of samples of wind and waves

In this section, the effect of varying numbers of wind and wave samples on the drivetrain 1-h fatigue damage is studied, with an aim to recommend a reasonable sample number for drivetrain dynamic simulation. The ensemble average of 1-h fatigue damage over 30 random wind and wave samples is used as the reference value, and this study is carried out based on the following expression:

$$\chi = \frac{\overline{D_i} - \overline{D_{30}}}{\overline{D_{30}} \times 100} \tag{15}$$

where $\overline{D_i}$ and $\overline{D_{30}}$ are the ensemble average of 1-h fatigue damage of bearings over i and 30 random samples, i represents 1, 2, 3, ... , 30. χ denotes the percentage difference of the ensemble average of bearing 1-h fatigue damage between the i and 30 random wind and wave samples.

Fig. 38 illustrates the deviations of the average 1-h fatigue damage of drivetrain over different numbers of wind and wave samples from the reference value over 30 samples under the rated environmental condition. It is observed the largest deviation of the drivetrain fatigue damage from the reference value is less than 5%, which suggests that the number of samples used for simulations does not significantly affect the fatigue damage. In general, the deviations of the fatigue damage in the main bearings are larger than that in the gearbox bearings, which implies that the number of samples used for simulations have a larger effect on drivetrain main bearings than that on bearings in the gearbox. When five samples are used, the percentage differences in the fatigue damage of the main bearings and the gearbox bearings are less than 2% and 1%, respectively. This implies that considering 5 wind and wave samples for drivetrain dynamic analysis can achieve accurate results and greatly save computational costs. Therefore, 5 random samples of wind and waves are recommended to be considered for drivetrain dynamic analysis.

5. Concluding remarks

This study investigates the effect of variability and uncertainty of environmental conditions on short-term fatigue damage in drivetrains of floating wind turbines. The global aero-hydro-servo-elastic dynamic analysis, for the DTU 10-MW wind turbine supported on the OO-Star semi-submersible floating substructure, is performed based on time-domain simulations that are conducted using the wind turbine simulation tool FAST. Then, the wind turbine drivetrain dynamic analysis is conducted with the applied hub and generator loads as well as nacelle motions that are obtained from the global simulations. Further, 1-h short-term fatigue damage of the drivetrain bearings is calculated based on the bearing dynamic responses. The influence of variations of mean wind speed, turbulence intensity, wind shear exponent, significant wave height and spectral peak period, wind and wave misalignment angle and the number of 1-h samples of wind and waves, on the 1-h drivetrain fatigue damage is studied. The main conclusions are summarized as follows:

- Below the rated conditions, the fatigue damage of bearings in the gearbox is very sensitive to the variation of mean wind speed because of the change of torque loads. Above the rated conditions, the variation of the mean wind speed has a great effect on fatigue damage of main bearings because of the variation of rotor bending moments, while other bearings are slightly affected. Because of the large variations of the rotor nontorque bending moments, torque loads and load cycles, fatigue damage of all bearings is significantly affected by the variation of the mean wind speed below and near the rated conditions.
- Fatigue damage in the main bearings increases approximately linearly with the turbulence intensity within a certain range in all environmental conditions. The effect of turbulence intensity on fatigue damage of main bearings is larger in more severe environmental conditions than in milder ones. In low wind-speed condition, the increases of turbulence intensity result in larger fatigue damage of high-speed bearings because of the increasing rotor torque. The variation of turbulence intensity does not affect fatigue damage in middle-speed bearings of the gearbox.
- The variation of the wind shear exponent significantly affects the fatigue damage of main bearings, while they have negligible impacts on fatigue damage of gearbox bearings. Fatigue damage of main bearings decreases approximately linearly with increasing the wind shear exponent within a certain range in all investigated environmental conditions. The effect of the variation of wind shear exponent on fatigue damage of main bearings increases as the environmental conditions become more severe.
- Fatigue damage in the main bearings increases slightly as the significant wave height increases because the nacelle pitch acceleration increases and consequently the global pitch bending moment of the drivetrain shaft increases. In addition, the effect of uncertainty of the spectral peak period on the drivetrain fatigue damage is very small.
- Although wind-wave misalignment causes quite small effects on drivetrain fatigue damage, the maximum and

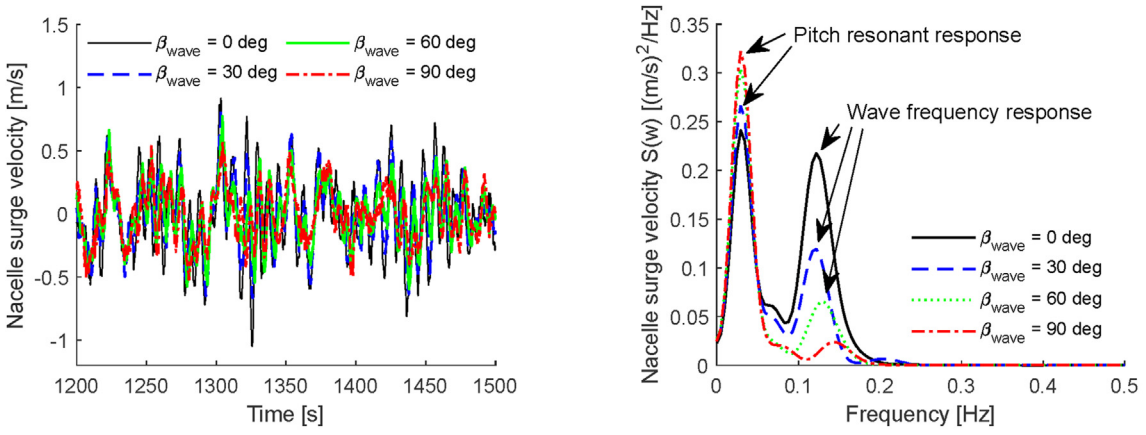

(a) Nacelle surge velocity

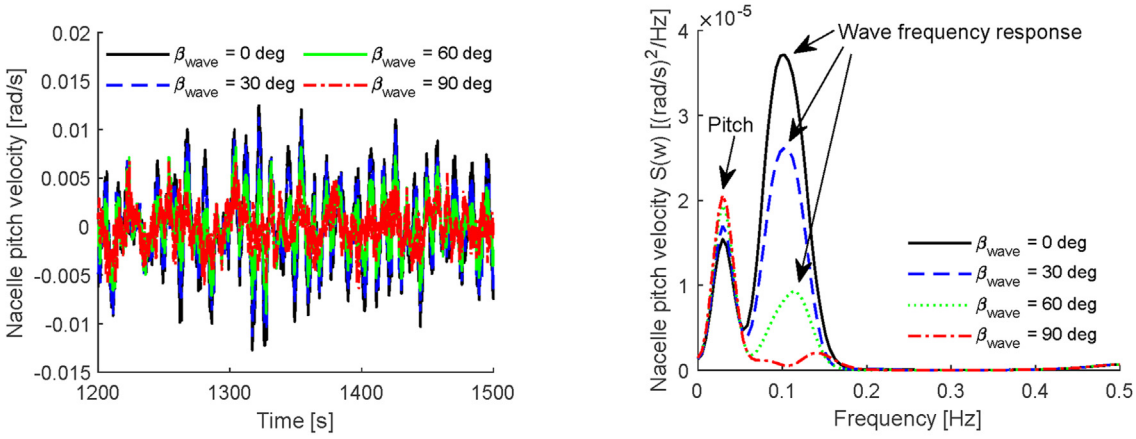

(b) Nacelle pitch velocity

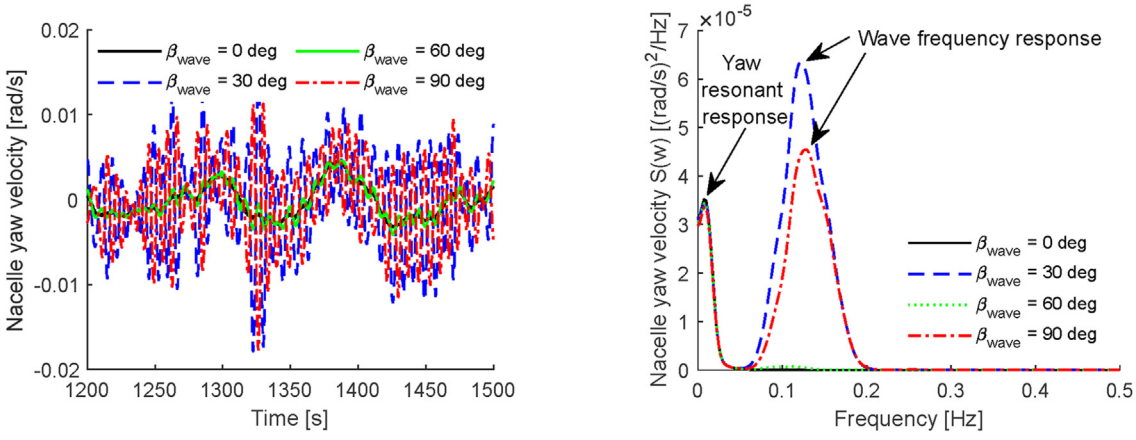

(c) Nacelle yaw velocity

Fig. 36. Comparison of time series and power spectra of nacelle surge, pitch and yaw velocities in 0 deg, 30 deg, 60 deg and 90 deg wave directions under above-rated environmental condition; refer to Fig. 5 for the coordinate system.

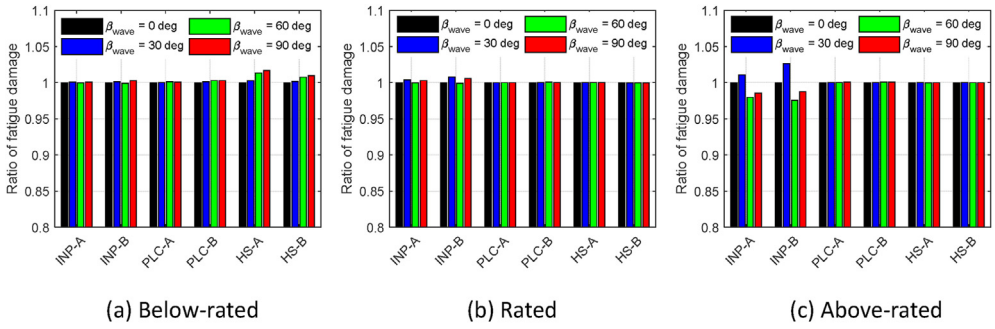

Fig. 37. Comparison of drivetrain 1-h fatigue damage in 0 deg, 30 deg, 60 deg and 90 deg wave directions under below-rated, rated and above-rated environmental conditions.

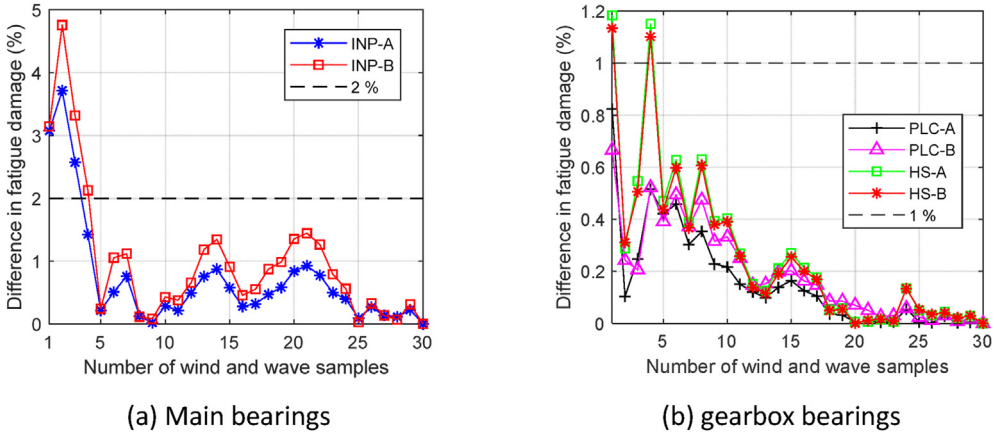

Fig. 38. Deviations of averaged 1-h fatigue damage of drivetrain over different numbers of wind and wave samples under rated environmental condition.

minimum fatigue damage of main bearings occur at 30 deg and 90 deg wind-wave misalignment conditions, respectively.

- To achieve a high accuracy of the drivetrain short-term fatigue damage, five independent 1-h simulations with random wind and wave samples are recommended.

Overall, variability and uncertainty of the stochastic wind field represent the main sources that determine the variation of drivetrain fatigue damage in the floating offshore wind turbines, while the effect of variabilities and uncertainties of irregular waves on the drivetrain fatigue damage is much smaller. Realistic wind fields should be applied based on meteorological data and wake effects in the wind farm when performing drivetrain design and reliability assessment for floating offshore wind turbines. Small wind speed bin sizes are recommended because they significantly affect the fatigue damage in drivetrain bearings. In addition, in order to reduce the computational efforts, conservative assumption can be made in dealing with uncertainties of irregular waves. For example, a few load conditions, considering the largest significant wave height under given wind speed, the most probable spectral peak period and the 30 deg wind and wave misalignment, can be used to obtain relatively conservative results, instead of using all load cases obtained by combing different wave parameters.

In the four-point support drivetrain configuration, the main bearings are generally the most sensitive components to variation of environmental parameters. Thus, more attention should be paid to them when the drivetrain is subjected to complex wind and wave excitation. It is emphasized that this study is only carried out for an axially symmetrical semi-submersible floating wind turbine. Further studies of the effect of variabilities and uncertainties in turbulent wind and irregular waves on drivetrain fatigue damage of wind turbines supported on different floating structures should be conducted in the future. In particular, the investigation should be carried out for floaters with different dynamic properties, and swell or currents can be included in the environmental conditions. In this study, the collective pitch control is assumed for the blades. Using an individual pitch control for the FWT might affect the results and should be studied in the future. In addition, the turbulence intensity is specified deterministically as a function of the mean wind speed. As a further refinement, its variability can be modeled in the same way as that of the significant wave height and spectral peak period.

Funding support

Research Council of Norway through Centre for Ships and Ocean Structures (CeSOS) and the Centre for Autonomous Marine Operations and Systems (AMOS, Norwegian University of Science and Technologyy. China Scholarship Council (CSC) (Grant No. 201706050147)

CRediT authorship contribution statement

Shuaishuai Wang: Conceptualization, Methodology, Software, Formal analysis, Writing – original draft, Writing – review & editing, Visualization. **Torgeir Moan:** Conceptualization, Methodology, Writing – review & editing, Supervision. **Zhiyu Jiang:** Conceptualization, Methodology, Writing – review & editing.

Declaration of competing Interest

The authors declare that they have no known competing financial interests or personal relationships that could have appeared to influence the work reported in this paper.

Acknowledgement

The first and second authors would like to acknowledge the support from the Research Council of Norway through Centre for Ships and Ocean Structures (CeSOS) and the Centre for Autonomous Marine Operations and Systems (AMOS, Norwegian University of Science and Technologyy. Moreover, the first author would like to thank the financial support from the China Scholarship Council (CSC) (Grant No. 201706050147).

References

[1] International Energy Agency (IEA), Offshore wind outlook. https://www.iea.org/reports/offshore-wind-outlook-2019, 2019. (Accessed 2 July 2020).
[2] F. Taveira-Pinto, P. Rosa-Santos, T. Fazeres-Ferradosa, Marine renewable energy, Renew. Energy 150 (2020) 1160–1164.
[3] Wind Europe, Floating Offshore Wind Energy–A Policy Blueprint for Europe, 2018.
[4] T. Fazeres-Ferradosa, P. Rosa-Santos, F. Taveira-Pinto, E. Vanem, H. Carvalho, J. Correia, Advanced Research on Offshore Structures and Foundation Design: Part 1, Proceedings of the Institution of Civil Engineers-Maritime Engineering, Thomas Telford Ltd, 2019, pp. 118–123.
[5] T. Moan, Z. Gao, E.E. Bachynski, A.R. Nejad, Recent advances in integrated response analysis of floating wind turbines in a reliability perspective, J. Offshore Mech. Arctic Eng. 142 (5) (2020).
[6] W.D. Musial, P.C. Beiter, P. Spitsen, J. Nunemaker, V. Gevorgian, Offshore Wind Technologies Market Report, National Renewable Energy Lab.(NREL), Golden, CO (United States), 2018, 2019.
[7] B. Wen, X. Tian, Q. Zhang, X. Dong, Z. Peng, W. Zhang, K. Wei, Wind shear effect induced by the platform pitch motion of a spar-type floating wind turbine, Renew. Energy 135 (2019) 1186–1199.
[8] M. Zhang, X. Li, J. Tong, J. Xu, Load control of floating wind turbine on a Tension-Leg-Platform subject to extreme wind condition, Renew. Energy 151 (2020) 993–1007.
[9] L. Zhang, W. Shi, M. Karimirad, C. Michailides, Z. Jiang, Second-order hydrodynamic effects on the response of three semisubmersible floating offshore wind turbines, Ocean Engineering 207 (2020) 107371.
[10] J.M. Hegseth, E.E. Bachynski, J.R. Martins, Integrated design optimization of spar floating wind turbines, Mar. Struct. 72 (2020) 102771.
[11] S. Faulstich, B. Hahn, P.J. Tavner, Wind turbine downtime and its importance for offshore deployment, Wind Energy 14 (3) (2011) 327–337.
[12] Caithness Windfarm Information Forum, Summary of wind turbine accident data to 30 september 2020. http://www.caithnesswindfarms.co.uk/AccidentStatistics.htm. (Accessed 15 November 2020).
[13] Y. Xing, M. Karimirad, T. Moan, Effect of spar-type floating wind turbine nacelle motion on drivetrain dynamics, in: Proceedings of EWEA 2012 Annual Event, 2012.
[14] S. Wang, A. Nejad, E.E. Bachynski, T. Moan, A comparative study on the dynamic behaviour of 10 MW conventional and compact gearboxes for offshore wind turbines, Wind Energy 24 (7) (2021) 770–789.
[15] Z. Li, B. Wen, K. Wei, W. Yang, Z. Peng, W. Zhang, Flexible dynamic modeling and analysis of drive train for Offshore Floating Wind Turbine, Renew. Energy 145 (2020) 1292–1305.
[16] IEC61400-4, International Electrotechnical Commission, Wind Turbines-Part 4: Design Requirements for Wind Turbine Gearboxes, 2012.
[17] IEC61400-1, International Electrotechnical Commission, Wind Turbines–Part 1: Design Requirements, 2005.
[18] IEC61400-3, International Electrotechnical Commission, Wind Turbines—Part 3: Design Requirements for Offshore Wind Turbines, 2009.
[19] C. Bak, F. Zahle, R. Bitsche, T. Kim, A. Yde, L.C. Henriksen, M.H. Hansen, J.P.A.A. Blasques, M. Gaunaa, A. Natarajan, The DTU 10-MW Reference Wind Turbine, Danish Wind Power Research 2013, 2013.
[20] W. Yu, K. Müller, F. Lemmer, D. Schlipf, H. Bredmose, M. Borg, T. Landbø, H. Andersen, LIFES50+ D4. 2: Public Definition of the Two LIFES50+ 10 MW Floater Concepts, University of Stuttgart, 2018.
[21] A. Pegalajar-Jurado, F. Madsen, M. Borg, H. Bredmose, LIFES50+ D4. 5: State-Of-The-Art Models for the Two LIFES50+ 10 MW Floater Concepts, Technical Report, Technical University of Denmark, 2018.
[22] Dr techn, A.S. Olav Olsen. https://www.olavolsen.no. (Accessed 6 July 2020).
[23] LIFES 50+ project. https://lifes50plus.eu. (Accessed 6 July 2020).
[24] A. Pegalajar-Jurado, H. Bredmose, M. Borg, J. Straume, T. Landbø, H. Andersen, W. Yu, K. Müller, F. Lemmer, State-of-the-art model for the LIFES50+ OO-Star Wind Floater Semi 10MW floating wind turbine, J. Phys. Conf. Ser (2018), 012024.
[25] S. Wang, A.R. Nejad, T. Moan, On design, modelling, and analysis of a 10-MW medium-speed drivetrain for offshore wind turbines, Wind Energy 23 (4) (2020) 1099–1117.
[26] S. Wang, A.R. Nejad, T. Moan, Design and dynamic analysis of a compact 10 MW medium speed gearbox for offshore wind turbines, J. Offshore Mech. Arctic Eng. 143 (3) (2021), 032001.
[27] S. Wang, A.R. Nejad, E.E. Bachynski, T. Moan, Effects of bedplate flexibility on drivetrain dynamics: case study of a 10 MW spar type floating wind turbine, Renew. Energy 161 (2020) 808–824.
[28] B. Jonkman, J. Jonkman, FAST V8. 16.00 A-Bjj, National Renewable Energy Laboratory, 2016.
[29] M. Hall, MoorDyn User's Guide, Department of Mechanical Engineering, University of Maine, Orono, ME, 2015.
[30] SIMPACK, Multi-body system software. https://www.3ds.com/products-services/simulia/products/simpack/, 2020. (Accessed 6 March 2020).
[31] SIMPACK User Assistance, Multi-body system software. https://www.3ds.com/products-services/simulia/products/simpack/, 2020. (Accessed 14 September 2021).
[32] W. LaCava, Y. Xing, Y. Guo, T. Moan, Determining Wind Turbine Gearbox Model Complexity Using Measurement Validation and Cost Comparison, National Renewable Energy Lab.(NREL), Golden, CO (United States), 2012.
[33] C. Zhu, S. Chen, H. Liu, H. Huang, G. Li, F. Ma, Dynamic analysis of the drive train of a wind turbine based upon the measured load spectrum, J. Mech. Sci. Technol. 28 (6) (2014) 2033–2040.
[34] Y. Guo, J. Keller, W. La Cava, J. Austin, A. Nejad, C. Halse, L. Bastard, J. Helsen, Recommendations on Model Fidelity for Wind Turbine Gearbox Simulations, National Renewable Energy Lab.(NREL), Golden, CO (United States), 2015.
[35] S. Wang, T. Moan, Dynamic behaviour comparison of a 10-MW drivetrain in a bottom-fixed Monopile and a spar floating wind turbines, in: The 30th International Ocean and Polar Engineering Conference, International Society of Offshore and Polar Engineers, 2020.
[36] S. Wang, T. Moan, A.R. Nejad, A comparative study of fully coupled and decoupled methods on dynamic behaviour of floating wind turbine drivetrains, Renew. Energy 179 (2021) 1618–1635.
[37] Z. Jiang, Y. Xing, W. Dong, T. Moan, Z. Gao, Long-term probability distribution of wind turbine planet roller bearing loads, in: WINDPOWER 2013 Conference & Exhibition, 2013, pp. 1–21.
[38] P.J. Moriarty, A.C. Hansen, AeroDyn Theory Manual, National Renewable Energy Lab., Golden, CO (US), 2005.
[39] J.M. Jonkman, A. Robertson, G.J. Hayman, HydroDyn User's Guide and Theory Manual, National Renewable Energy Laboratory, 2014.
[40] I. Wamit, Wamit User Manual, Chestnut Hill, USA, 2006.
[41] W. Cummins, The Impulse Response Function and Ship Motions, David Taylor Model Basin, Washington DC, 1962.
[42] ISO281, Dynamic Load Ratings and Rating Life, International Organization for Standardization, Geneva, Switzerland, 2007.
[43] L. Li, Z. Gao, T. Moan, Joint distribution of environmental condition at five european offshore sites for design of combined wind and wave energy devices, J. Offshore Mech. Arctic Eng. 137 (3) (2015).
[44] Z. Jiang, Y. Xing, Y. Guo, T. Moan, Z. Gao, Long-term contact fatigue analysis of a planetary bearing in a land-based wind turbine drivetrain, Wind Energy 18 (4) (2015) 591–611.
[45] B.J. Jonkman, TurbSim User's Guide: Version 1.50, National Renewable Energy Lab.(NREL), Golden, CO (United States), 2009.
[46] G.C. Larsen, K. Ronold, H.E. Jørgensen, K. Argyriadis, J. de Boer, Ultimate Loading of Wind Turbines, RISO-REPORTS-RISO R, 1999.
[47] X. Chen, Z. Jiang, Q. Li, Y. Li, N. Ren, Extended environmental contour methods for long-term extreme response analysis of offshore wind turbines, J. Offshore Mech. Arctic Eng. 142 (5) (2020).
[48] M. Türk, S. Emeis, The dependence of offshore turbulence intensity on wind speed, J. Wind Eng. Ind. Aerod. 98 (8–9) (2010) 466–471.
[49] M.H. Myrtvedt, A. Nybø, F.G. Nielsen, The dynamic response of offshore wind turbines and their sensitivity to wind field models, J. Phys.: Conference Series, IOP Publishing (2020), 012013.
[50] A. Nybø, F.G. Nielsen, J. Reuder, M.J. Churchfield, M. Godvik, Evaluation of different wind fields for the investigation of the dynamic response of offshore wind turbines, Wind Energy 23 (9) (2020) 1810–1830.
[51] B. Ernst, J.R. Seume, Investigation of site-specific wind field parameters and their effect on loads of offshore wind turbines, Energies 5 (10) (2012) 3835–3855.
[52] A. Nybø, F.G. Nielsen, J. Reuder, Processing of sonic anemometer measurements for offshore wind turbine applications, J. Phys.: Conference Series, IOP Publishing (2019), 012006.
[53] M. Kretschmer, V. Pettas, P.W. Cheng, Effects of Wind Farm Down-Regulation in the Offshore Wind Farm Alpha Ventus, International Conference on Offshore Mechanics and Arctic Engineering, American Society of Mechanical Engineers, 2019. V001T01A032.
[54] T. Burton, D. Sharpe, N. Jenkins, E. Bossanyi, Wind Energy Handbook, Wiley Online Library, 2001.
[55] M. Tuerk, K. Grigutsch, S. Emeis, The Wind Profile above the Sea. Investigations Basing on Four Years of FINO 1 Data; Das Windprofil Ueber See, Auswertung von vier Jahren FINO 1-Daten, 2008.
[56] E.E. Bachynski, M.I. Kvittem, C. Luan, T. Moan, Wind-wave misalignment effects on floating wind turbines: motions and tower load effects, J. Offshore

Mech. Arctic Eng. 136 (4) (2014).
[57] L. Barj, J.M. Jonkman, A. Robertson, G.M. Stewart, M.A. Lackner, L. Haid, D. Matha, S.W. Stewart, Wind/wave misalignment in the loads analysis of a floating offshore wind turbine, in: 32nd ASME Wind Energy Symposium, 2014, 0363.
[58] T. Fischer, P. Rainey, E. Bossanyi, M. Kühn, Study on control concepts suitable for mitigation of loads from misaligned wind and waves on offshore wind turbines supported on monopiles, Wind Eng. 35 (5) (2011) 561–573.